Dry deposition of airborne trace metals on the Los Angeles Basin and adjacent coastal waters

R. Lu, R. P. Turco, K. Stolzenbach, S. K. Friedlander, and C. Xiong
Institute of the Environment, University of California, Los Angeles, California, USA

K. Schiff and L. Tiefenthaler
Southern California Coastal Water Research Project, Westminster, California, USA

Guangyu Wang
Santa Monica Bay Restoration Project, Los Angeles, California, USA

Received 31 October 2001; revised 19 March 2002; accepted 16 April 2002; published 31 January 2003.

[1] We present an assessment of the deposition rates of airborne trace metals onto the Los Angeles Basin and adjacent coastal waters. For this purpose, the UCLA Surface Meteorology and Ozone Generation (SMOG) air pollution modeling system has been used to simulate the geographical distributions of trace metals and their deposition fluxes. Calculations were performed for average summer and winter conditions, as well as for extreme meteorological events, in particular, for Santa Ana winds. Thus, a series of simulations were carried out that define the range of meteorological conditions contributing to dry deposition in the region. These predictions have been calibrated and validated using measurements collected in the LA area. Significant spatial and temporal variability are found in trace metal concentrations and deposition rates. Large spatial gradients occur near the coast as well as at the mountainous boundaries of the airshed. Considerable diurnal and seasonal variations in trace metal deposition are also noted. For example, the development of a daytime sea breeze, particularly in the warmer months, leads to greater deposition in the northern and eastern basin as well as in the high desert. A nighttime land breeze, especially in the colder months, enhances deposition onto coastal ocean surfaces. Large particles dominate local trace metal deposition in central urban (and adjacent) areas, while fine particles export metals over regional scales through long-range advection. Since the majority of urban metal deposition occurs on particles larger than 10-μm diameter, routine measurements of PM_{10} or $PM_{2.5}$ concentrations for air quality characterization may not be reliable indicators of local sources. Some 35–45% of all trace metal emissions are deposited locally within the Los Angeles Basin on an annual basis. Santa Monica Bay and its watersheds receive about 6% of this amount, which can have a significant impact on trace metal concentrations in the surface waters of the bay, primarily through land runoff following storms. *INDEX TERMS:* 0345 Atmospheric Composition and Structure: Pollution—urban and regional (0305); 0305 Atmospheric Composition and Structure: Aerosols and particles (0345, 4801); 0368 Atmospheric Composition and Structure: Troposphere—constituent transport and chemistry; 0312 Atmospheric Composition and Structure: Air/sea constituent fluxes (3339, 4504)

Citation: Lu, R., R. P. Turco, K. Stolzenbach, S. K. Friedlander, C. Xiong, K. Schiff, L. Tiefenthaler, and G. Wang, Dry deposition of airborne trace metals on the Los Angeles Basin and adjacent coastal waters, *J. Geophys. Res.*, *108*(D2), 4074, doi:10.1029/2001JD001446, 2003.

1. Introduction

[2] Urban air generally contains significantly higher trace metal concentrations than air in rural areas, owing mainly to emissions from industrial activities, energy generation and vehicular traffic. Highly toxic metals carried on aerosols are continuously released in large quantities, which may have long-term ecological and health implications. Deposition of metal-bearing particles onto surfaces (dry deposition) is an important mechanism controlling the fate of airborne metals. The particulates may become attached to plant and other surfaces, trapped within soil matrices, or entrained into the surface microlayer film covering coastal and inland waters and wetlands. Significant contamination and ecological impacts might be expected in highly polluted urban areas such as the Los Angeles Basin. Effective management of this pollution requires accurate knowledge of atmospheric deposition fluxes and patterns, as well as source-receptor relationships.

[3] Aerosols in the ambient air of greater Los Angeles are known to contain many toxic constituents, as well as nu-

0148-0227/03/2001JD001446$09.00

trients that can eutrophy marine ecosystems [*Arey et al.*, 1989; *Young et al.*, 1976]. Moreover, atmospheric deposition is well recognized as a potentially significant non-point source of contaminants to water bodies [*Baker*, 1997]. Yet, over the years, only a relatively small number of studies have addressed the problem of aerosol deposition on the coastal waters of Los Angeles. For example, *Kaplan and Lu* [1993] estimated the deposition of airborne organic and inorganic contaminants onto Santa Monica Bay. They used measured atmospheric concentrations over land, and assumed that all of the contaminant mass within a certain distance of the coastline would be deposited on the Bay. Kaplan and Lu concluded that atmospheric deposition was significant relative to other discharges to Santa Monica Bay for nickel, zinc, arsenic, selenium, cadmium, mercury, and lead. *Eaganhouse and Venkatesan* [1993] employed measurements of carbon compounds by *Gray et al.* [1986] and rough deposition velocities to compute the quantities of carbon compounds deposited throughout the region. *Huntzicker et al.* [1975] estimated that out of a total 17.9 metric tons/day of lead emitted by mobile sources, the coastal waters received 0.43 tons/day in runoff from streets, 0.3 tons by regional dry deposition, and 0.09 tons by regional wet deposition. This total of 0.81 tons/day reaching the coastal waters exceeded the 0.64 tons/day estimated as the contribution from sewage discharges. In an update to this study, *Lankey et al.* [1998] determined that although the total quantity of lead emitted had been greatly reduced, the relative quantities of local (street) deposition, regional deposition, and removal by wind were approximately the same as in the earlier study.

[4] Because of the relatively small annual rainfall in Los Angeles, studies of atmospheric deposition have focused primarily on dry deposition processes. Useful in this regard are a number of measurements of particulate-borne trace metals conducted in the L.A. area. Trace metal content is often used to characterize urban aerosols [*Davidson and Osborn*, 1986; *Milford and Davidson*, 1985], and to quantify the contributions of different particle sources at receptor sites, through chemical mass balance techniques [e.g., *Cass and McRae*, 1986; *Lyons et al.*, 1993]. Nevertheless, relatively few studies of actual trace metal deposition rates in the Los Angeles airshed have been carried out. There has been little direct monitoring of atmospheric deposition, for example. *Davidson* [1977] recorded the dry deposition rates of several trace metals (Pb, Zn, and Cd) on flat Teflon plates while simultaneously monitoring the aerosol mass size distribution with a cascade impactor. He found that the sedimentation of large particles accounted for about 70% of the total mass deposition over a flat surface (in Pasadena, California). Focusing on vegetative surfaces, *Davidson and Friedlander* [1978] concluded that impaction controls the dry deposition of these three metals, with ~90% of the deposited lead, and even greater fractions of Zn and Cd, resulting from the impaction of particles larger than 10 μm. This implies that estimates of deposition rates based on PM_{10} data (that is, the total mass concentration of airborne particulate matter in particles with diameters below 10 μm), which are typically used to characterize air quality against established standards, will not be reliable [*Holsen et al.*, 1993].

[5] Basic dry deposition processes have been investigated both theoretically and experimentally (see *Pryor and Barthelmie* [2000] for a recent review). Experimentally, artificial surfaces are used to collect aerosols, and to characterize the original nature of the deposited materials [e.g., *Franz et al.*, 1998; *Paode et al.*, 1998, 1999; *Shahin et al.*, 2000; *Tai et al.*, 1999; *Yi et al.*, 1997a, 1997b]. When the properties of the particles above the collector are carefully monitored, the effective deposition velocity to the plate can be determined [e.g., *Caffrey et al.*, 1998; *Holsen et al.*, 1993; *Tanner et al.*, 2001; *Yi et al.*, 2001; *Zufall et al.*, 1998]. Based on such results, dry deposition velocities may be computed for a wider range of conditions using appropriate theoretical formulations for land [e.g., *McRae et al.*, 1982; *Zhang et al.*, 2001] and water surfaces [e.g., *Lo*, 1993; *Lo et al.*, 1999; *Slinn and Slinn*, 1980; *Williams*, 1982] (also see *Zufall and Davidson* [1997] for a recent review).

[6] Owing to the difficulties involved in characterizing aerosols and deploying collection surfaces in the field, experimental studies in situ have usually been limited in duration and spatial extent. However, significant gradients in atmospheric deposition patterns have been noted in cities [e.g., *Lovett et al.*, 2000; *Tai et al.*, 1999]. Since sampling at individual sites cannot adequately describe atmospheric deposition across large and topographically diverse urban areas and watersheds [*Lovett et al.*, 1997], the extrapolation of "point" measurements to urban and regional scales is inherently difficult. As an alternative, theoretical algorithms based on experimental results may be used to calculate dry deposition fluxes in an air quality model that resolves spatial variations in particulate properties, leading to a more self-consistent assessment of the regional-scale deposition of airborne contaminants.

[7] The present work describes a methodology for determining aerosol dry deposition rates across the Los Angeles Basin, focusing on trace metal deposition onto coastal waters and watersheds. To achieve our objectives, a three-dimensional air quality model, Surface Meteorology and Ozone Generation (SMOG), is employed to simulate the atmospheric loadings and dry deposition patterns of particulate-borne trace metals across the region. In section 2, the capabilities of the SMOG model for performing trace metal deposition studies are outlined. Here, detailed treatments of meteorology, pollutant dispersion, gas-phase photochemistry, and aerosol microphysics and chemistry are described. Comparisons between model predictions and recent measurements of trace metal distributions (for Al, As, Cd, Cr, Cu, Fe, Mn, Ni, Pb, Zn) are presented in section 3. The computational results are interpreted in section 4, and conclusions are offered in section 5.

2. The Smog Modeling System

[8] The SMOG air quality model was originally developed to study gaseous and particulate pollutants in the Los Angeles Basin (LAB) [*Lu et al.*, 1997a; *Jacobson*, 1997; *Jacobson et al.*, 1996a]. The model couples meteorological, radiative, chemical, and microphysical processes in a consistent way. Because of its generalized and modular structure, the model can be used to address a wide range of scientific problems, and to develop strategies for regulating urban and regional air pollution. The performance of the SMOG modeling system has been evaluated by comparing predictions against measurements collected during the Southern California Air Quality Study (SCAQS) and other

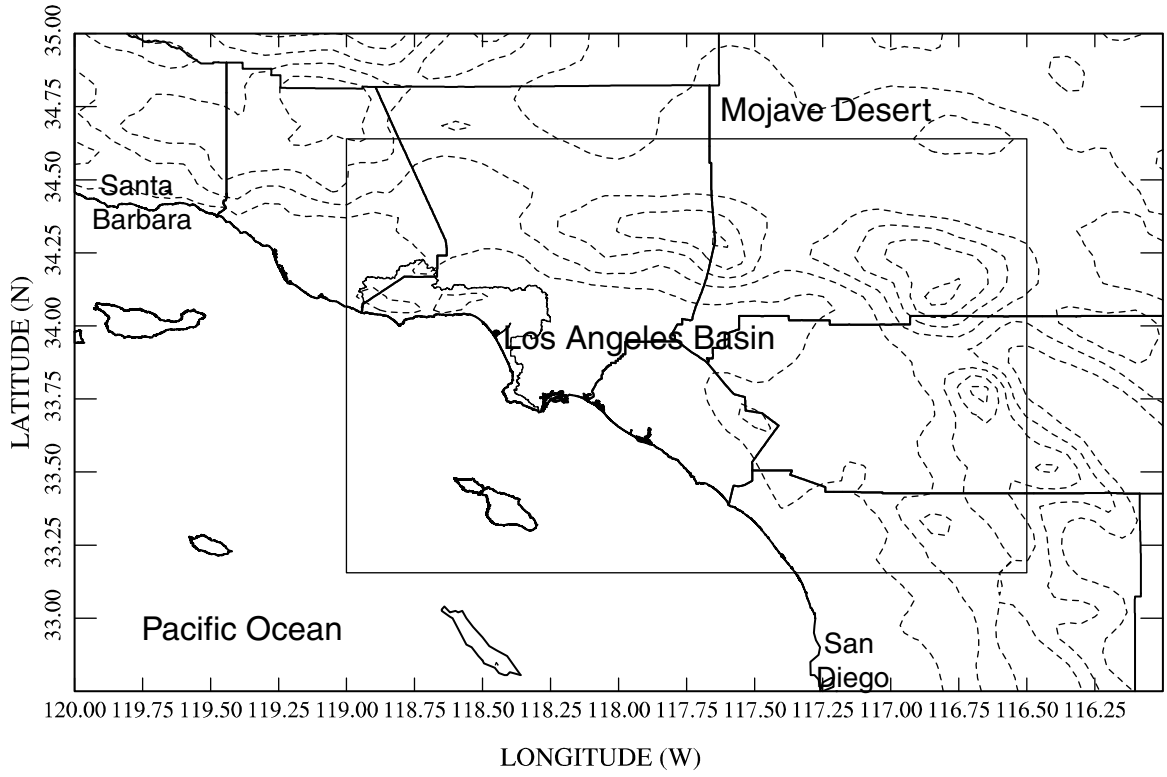

Figure 1. Model simulation domains for the present study. The outer domain is used for the meteorological simulation, and the configurable inner domain is employed for the air quality predictions. For the simulation of Santa Ana wind conditions, the inner domain is expanded over the ocean surface. Thick lines represent coastal and county boundaries. Dashed contours define terrain elevations at intervals of 400 m.

intensive field campaigns [*Lu et al.*, 1997b]. From these comparisons, it has been demonstrated that the model accurately reproduces the key features of regional meteorology, pollutant dispersion, and chemical transformations in LAB. For the present work, we include a comprehensive treatment of gas-phase photochemistry and aerosol microphysics, as described in earlier publications [e.g., *Jacobson and Turco*, 1994; *Jacobson et al.*, 1996a; *Lu et al.*, 1997a].

[9] In the present simulations, the model domain covers the entire southern California area, with a configurable inner domain used for the air quality calculations (Figure 1) [*Lu et al.*, 1997a]. The nominal uniform grid spacing is 0.050° longitude × 0.045° latitude (roughly 4.6 × 5 km), and applies to both the outer and nested grids. In the vertical direction, variable grid spacing is used with higher resolution in the boundary layer. Meteorological parameters, including wind vectors, temperature, pressure and relative humidity, are predicted over the larger domain (with 85 × 55 × 20 grid cells). The inner domain is focused on the LAB itself. For normal summer and winter conditions, the appropriate inner domain is shown in Figure 1; however, during Santa Ana conditions, when pollutants emitted in the basin can be transported far offshore, this domain is extended over a much larger area of the adjacent ocean surface.

2.1. Metal Size Distributions

[10] In order to calculate the deposition fluxes of trace metals onto the Los Angeles Basin and Santa Monica Bay, the SMOG model has been configured to simulate the dispersion of inert particulate-borne trace metals from emission sources, as well as their deposition rates over land and water surfaces. Aerosol sizes are resolved into 12 diameter bins, defined in Table 1, covering the range from 0.01 to 40 μm. For the present work, the aerosol is characterized by one internally mixed particle type having 34 components, with each component defined by its volume fraction in each size class. The main components include the metals of interest (Al, As, Cd, Cr, Cu, Fe, Mn, Ni, Pb, Zn) as well as nitrate, sulfate, sea salt, organic and elemental carbon, and water. Although a significant number of species are tracked, the present representation is still relatively simple for an urban

Table 1. Discrete Aerosol Size Bins Used in the Present Simulations

Bin	Mean Diameter, μm	Lower Boundary, μm	Upper Boundary, μm
1	0.017	0.010	0.020
2	0.033	0.020	0.040
3	0.066	0.040	0.080
4	0.131	0.080	0.158
5	0.261	0.158	0.316
6	0.520	0.316	0.630
7	1.038	0.630	1.257
8	2.069	1.257	2.506
9	4.126	2.506	4.997
10	8.228	4.997	9.964
11	16.41	9.964	19.871
12	32.72	19.871	39.625

aerosol. The fixed size bins in Table 1 correspond to the equivalent "dry" aerosol, consisting of all of the volatile and nonvolatile components except water. In practice, the model predicts the concentration and composition of the particles in each size bin, at every spatial cell in the three-dimensional regional domain. The water content of the particles in a given size/space bin changes with ambient relative humidity [*Jacobson and Turco*, 1995]. The corresponding "wet" aerosol sizes are used to calculate coagulation, sedimentation and deposition rates [*Jacobson et al.*, 1996b].

[11] Since the trace metals are considered as inert aerosol components in this study, gaseous and aqueous phase chemical processes involving the metals do not directly affect their abundances. Such reactions, however, can change the oxidation state and solubility of the metals, although such effects are neglected here. To further simplify the microphysical calculations, aerosol emissions were "preprocessed" to reflect the time required for local emissions to disperse to the regional SMOG grid. In particular, the primary nucleation and coagulation processes in local plumes that are not explicitly resolved by the model are presumed to reach quasi-equilibrium as the aerosol disperses over several kilometers. Accordingly, local processing cannot be analyzed using the present simulations. For example, rapid nucleation of metal vapors immediately after emission from high temperature combustion sources must be implicitly accounted for through the choice of an initial size distribution for these particles. Similarly, coagulation contributes to the evolution of particles below roughly one micron in the densest plumes originating from point sources. Such subgrid scale transformations are incorporated into the size and composition characterization of the area-weighted particle emissions over a model cell, as discussed later in this section.

[12] Metal particulates may also be transferred from small size bins into the accumulation mode by gas-to-particle conversion, especially condensation of sulfate and nitrate [e.g., *Hering and Friedlander*, 1982]. In the simulations carried out here, this effect is treated empirically by using metal mass distributions determined experimentally for LAB particulates [*Lyons et al.*, 1993]. In this case, each metal is initially distributed into size bins according to its observed size dispersion. While this approach works well for many of the species of interest, there is insufficient information available to treat every metal (e.g., Cr). In these latter cases, the metals are assumed to have "grown" into larger bins in the same manner as an analog species (e.g., Zn as an analog for Cr). While this approach cannot accurately represent the aerosol in close proximity to concentrated sources, it does provide a consistent characterization of the dispersed aerosol across the LAB. Indeed, given other uncertainties in the sources, quantities and rates of condensing compounds (organics, for example) an empirical representation is justified at this time. Such an approach also eliminates, in principle, the need to calculate explicitly the rates of transformation and condensation of inorganic compounds. Nevertheless, we have also carried out fully interactive chemical/aerosol simulations (discussed later) to test the sensitivity of our results to the initialization procedure. It should be noted at this point that the empirical assumptions described above have only a marginal influence on the conclusions ultimately drawn below, while greatly reducing the computational burden of the present aerosol simulations. Fully interactive microphysics and chemistry is included, however, in related studies of the nitrate cycle in the LAB (R. Lu and R. P. Turco, manuscript in preparation, 2003).

2.2. Dry Deposition Calculation

[13] The dry deposition fluxes, F, of gases and particles from the atmosphere to the surface are assumed to be proportional to the concentration, C, and deposition velocity, v_d, at a reference height (lying at about 20 m above the surface, which is the middle of the lowest model layer in this study). Thus,

$$F = -v_d C. \tag{1}$$

[14] The physical model used to calculate dry deposition velocities is based on an "electrical resistance" analog, where the "voltage" is the vapor concentration and the "current" is the molecular flux across the region of interest. The deposition velocity for gases at the reference height is then defined as the inverse of the total resistance to pollutant deposition,

$$v_d = \frac{1}{r_1} = \frac{1}{r_a + r_b + r_s}. \tag{2}$$

The total resistance is the sum of the resistance, r_a, due to turbulent transport through the overlying atmosphere to the laminar viscous surface layer; the resistance, r_b, related to molecular scale diffusive transport through the viscous surface sublayer; and the resistance, r_s, associated with the uptake of the pollutant gas molecules at the surface. The surface resistance is a function of surface type and the reactivity of the depositing vapor with the surface material, and may be expressed as an "accommodation" coefficient.

[15] Here, and in equation (3) below, the turbulent resistance, r_a, is controlled by atmospheric stability and calculated based on the similarity theory. The resistance of the viscous sublayer, r_b, depends on the dimensionless Schmidt number, Sc [*Wesely et al.*, 1977], which is defined as $Sc = \upsilon/D$, where υ is the kinematic viscosity of air and D is the molecular diffusivity in air. Then, for a specific vapor, $r_b = \frac{2}{\kappa u_*} Sc^{2/3}$, where u_* is the surface friction velocity and κ is the von Karman constant.

[16] In the case of particle dry deposition, the effects of Brownian diffusion, inertial impaction, and particle gravitational sedimentation are accounted for in addition to turbulent transport and surface accommodation. If particles adhere to the surface upon contact without resuspension (i.e., $r_s = 0$), the dry deposition velocity can be written as [*Seinfeld and Pandis*, 1997],

$$v_d = \frac{1}{r_a + r_b + r_a r_b v_g} + v_g, \tag{3}$$

where v_g is the particle gravitational settling velocity. This velocity is calculated following the approach of *Toon et al.* [1989]. For particles, r_b depends on the effects of both Brownian diffusion and inertial impaction, $r_b = \frac{\kappa U}{u_*^2 (Sc^{-2/3} + 10^{-3/St})}$, where U is the wind speed. For the sizes

of interest, the Stokes number, St, is defined as, $St = v_g u_*^2/g\upsilon$, and g is the acceleration of gravity [$g = 9.81$ m s^{-2}].

[17] Over ocean surfaces, particle dry deposition velocities are calculated using the model of *Williams* [1982], which takes into account the effects of wave breaking and spray formation in high winds, and particle growth in the humid sublayer near the air/water interface. Using the electrical resistance approach, two parallel deposition paths are included in addition to gravitational settling. One pathway determines the rate of deposition across the turbulent layer and viscous sublayer onto areas characterized by smooth water surfaces. The second path controls the rate of deposition onto water surfaces affected by spray and bubbles. The fractional areas of each type of water surface are determined by the wind speed (see below). A lateral resistance, r_m, is also employed to represent the horizontal transfer between areas having smooth and broken surfaces. Gravitational settling in the viscous sublayer is adjusted for particle growth due to the higher relative humidity near the water surface. Over fresh water, the relative humidity may approach 100%, while over the ocean surface it is limited to about 98.3% owing to dissolved salts [*Williams*, 1982]. In this study, wet particle diameters in the viscous sublayer are estimated using the formula of *Fitzgerald* [1975], assuming a fixed relative humidity of 98% at the ocean surface, and a mean aerosol composition equivalent to ammonium nitrate. The fraction, α, of the surface area that is broken is given by,

$$\alpha = 1.7 \times 10^{-6} U_{10}^{3.75}. \quad (4)$$

where U_{10} is the wind speed at a reference height 10 m above the surface.

[18] The turbulent and sublayer resistances over smooth water surfaces are evaluated in a manner as described earlier in this section. The lateral resistance between the smooth and broken ocean areas is set to the same value as the turbulent resistance over a smooth water surface. Little is known about the sublayer resistance for broken surfaces. A tentative value of 0.1 s cm^{-1} [*Williams*, 1982] is used in the current study. When this resistance is equated to that corresponding to smooth surfaces, the deposition model collapses to the treatment of *Slinn and Slinn* [1980], without the effects of slip at the water surface.

[19] A key parameter that determines the surface aerodynamic state is the surface roughness height. A surface roughness data set from the Southern California Air Quality Management District (SCAQMD) is used here to characterize land surfaces. The surface of open oceans can be treated as aerodynamically smooth at low wind speeds ($U_{10} < 3$ m s^{-1}) and fully rough at high wind speeds ($U_{10} > 7$ m s^{-1}), with a transition region between these wind speeds [*Garratt*, 1977; *Wu*, 1969]. Following *Garratt* [1977] and *Giorgi* [1986], we estimate the value of the aerodynamic roughness height over the ocean using [*Charnock*, 1955],

$$z_0 = \beta \frac{u_*^2}{g} \quad (5)$$

where $\beta = 0.0144$ and g the gravity constant. This formula has been found to yield good agreement with observational data for $U_{10} < 25$ m s^{-1}. The friction velocity is estimated as $u_* = C_{DN}^{1/2} U \approx 0.023 U_{10}^{1.23}$ in the range $4 < U_{10} < 21$ m s^{-1} [*Garratt*, 1977]. Hence,

$$z_0 = 7.5 \times 10^{-7} U_{10}^{2.46} \quad (6)$$

(where U_{10} is in m s^{-1} and z_0 in meters). The roughness height is assumed to be limited at high wind speeds to a value of 0.024 m.

Table 2. Total Los Angeles Basin Emission Inventory for 1998[a]

Source	On-Road Mobile	Off-Road and Area	Point	Total
CO	3426.65	1440.17	141.60	5008.42
NOx	588.16	365.40	134.11	1087.66
SOx	14.21	43.27	22.84	80.32
VOC	448.09	1020.18	218.37	1686.63
PM	26.34	1392.04	22.61	1441.00
TOTAL	4503.45	4261.06	539.52	9304.03

[a] Emission rates are in tons/d.

3. Simulations of Trace Metal Concentrations and Distributions in the LA Basin

3.1. Standard Emission Inventory

[20] The inventories of gaseous and particulate emissions used in the present study have been compiled by the Southern California Air Quality Management District (SCAQMD) for 1998. The inventory consists of on-road mobile sources, off-road mobile and area sources, and major point sources. The emission inventory for on-road mobile sources, including cars, trucks, buses and motorcycles, is a product of the CARB EMFAC7G model with emission factors determined for 1998. The distributed and off-road sources are quite diverse, and represent best estimates by the SCAQMD. Area sources, for example, include dry cleaning establishments, gasoline stations, auto body shops and metal plating operations; off-road sources include construction equipment, ships and aircraft. Among the stationary point sources are a variety of industrial facilities and power plants.

[21] The 1998 inventory provides emission rates for CO, NO_x, SO_x, VOCs, and particulate matter (PM) for a wide range of source categories identified by the Source Classification Codes (SCCs). The emissions are spatially resolved on a 5 km $\times$ 5 km grid covering the South Coast Air Basin. Temporal variations in the emission rates are characterized using detailed hourly, daily (over a week) and monthly profiles. Table 2 summarizes the 1998 emission inventory as a yearly, mean 24-hour average input to the LAB. In each source category, emission inventories for individual volatile organic compounds and aerosol components are obtained by applying the latest CARB VOC and PM speciation profiles to the total VOC and PM emissions for that category. The on-road mobile PM emissions for 1998 are assigned as follows: 40.6% from diesel exhaust, 9.1% from gasoline exhaust, and 50.3% from tire and brake wear, based on studies for the Los Angeles county (X. Zhang, personal communication). The total PM mass emission is partitioned into four cumulative size fractions; i.e., for diameters <1 μm, <2.5 μm, <10 μm, and the total emission. Each chemical species is assigned a fraction of the cumulative mass at each size cut. Hence, the emissions into the standard size bins (that is, <1 μm, 1–2.5 μm, 2.5–10 μm

and >10 μm diameter) is calculated by differencing the cumulative masses, which is done for each species. Due to occasional inconsistencies between the cumulative PM masses and the species size fractionation profiles, small negative masses can occur in certain cases. A correction scheme is used to eliminate any negative mass fractions by adjusting the bin fractions sequentially from the smallest to the largest bin, while imposing overall mass balance. Although this procedure introduces errors into the absolute masses of the corrected species in the targeted size bins, our analysis shows there is a negligible impact on the results reported below.

[22] An example of trace metal cumulative PM mass emission rates on a weekday in August 1998 is shown in Table 3. The high emissions of aluminum and iron are associated with mineral dust lifted by winds and off-road traffic. Significant fractions of the emissions of chromium and nickel are connected with metallurgical works, while combustion sources emit substantial abundances of lead as well.

3.2. Size Resolution of Emissions

[23] To carry out the SMOG simulations, the size-resolved emissions need to be interpolated to the 12 model size bins defined in Table 1. The particle mass emitted in the range >10 μm diameter, for example, can be evenly partitioned across two model bins (11 and 12). Similarly, the particle mass in the range 2.5–10 μm may be allocated evenly to bins 9 and 10. In these cases, the mass injected into a bin is proportional to the width of the bin. For bins 7 and 8, the procedure is only slightly modified. The total mass emission in the interval from 1 to 2.5 μm is uniformly distributed across that interval, and then allocated to each bin according to the fractional overlap with that interval.

[24] Unfortunately, the standard emissions database does not resolve the "nucleation" mode characteristic of many particulate sources (in which typical particle diameters are <0.1 μm), especially combustion and metallurgical sources. In fact, all particles below 1 μm are lumped together in the available inventory, and this range is dominated by the "accumulation" mode. Observations in the LAB [e.g., *Whitby and Sverdrup*, 1980] show that the accumulation mode has a typical volume-weighted (or mass-weighted) mean diameter of about 0.32 μm, and standard deviation (for an equivalent lognormal distribution) of 2.16. The measurements also indicate that the volume of the nucleation mode is only a few percent of the volume of the accumulation mode [*Whitby and Sverdrup*, 1980]. In short, emissions into the nucleation mode cannot be explicitly resolved using the current inventory data.

[25] Automobiles and trucks are probably the greatest source of nucleation mode aerosols in Los Angeles. The emissions inventory, however, already averages these sources over an area roughly corresponding to a model grid cell. During the time interval required for the ultrafine particles to disperse over such distances (with travel times up to an hour), the smallest particles would be efficiently scavenged by background accumulation mode particles. For example, the coagulation lifetime of a 0.01 μm nucleation mode particle is about 20 min with a typical background concentration of 10^4 cm^{-3} accumulation mode particles. Accordingly, to initialize the $PM_{1.0}$ emissions over the spatial scales of interest, the total particulate output at sizes less then 1 μm is incorporated into a single primary accumulation mode aerosol. This particle mass is allocated to the model size bins smaller than 1 μm using a lognormal size distribution having the observed urban accumulation mode parameters discussed above (also see below). The size distribution function is truncated at an upper diameter of 1 μm (in bin 7), and the number of particles of given type is renormalized to conserve the total mass of that species in the size range <1 μm. Because all of the PM species are assumed to be commingled within a single mixed aerosol, it is not necessary to differentiate between internally and externally mixed particles at this point. The speciation among the totality of particles emitted into the bins covering the range from 0.01 to 0.63 μm (bins 1–6 in Table 1) is therefore assumed to be uniform. Bin 7, on the other hand, receives contributions from two standard inventory size ranges, and thus deviates from this rule. The procedure just outlined is used for many of the trace metals of interest here, with a few exceptions noted later.

[26] A number of measurements of the distributions of trace metals on particles as a function of particle size have

Table 3. Basin-Wide PM Trace Metal Emission Rates for a Typical August Weekday[a]

Elements	PM Size	On-Road Mobile	Area and Off-road Mobile	Point	All Sources
Al	Total	3.34	73,685.38	8.35	73,697.05
	<10 μm	1.81	47,281.54	2.59	47,285.95
	<2.5 μm	0.03	8,852.69	1.67	88,54.39
	<1 μm	0.03	2,483.62	1.06	2,484.7
As	Total	0.04	20.51	11.54	32.09
	<10 μm	0.04	14.64	10.42	25.11
	<2.5 μm	0.04	6.96	10.26	17.26
	<1 μm	0.04	5.2	10.13	15.37
Cd	Total	0.72	23.38	3.18	27.28
	<10 μm	0.55	18.74	3.04	22.33
	<2.5 μm	0.55	5.4	2.51	8.45
	<1 μm	0.13	4.27	2.43	6.82
Cr	Total	1.31	244.09	30.53	275.92
	<10 μm	1.3	139.2	28.96	169.45
	<2.5 μm	1.2	75.49	27.85	104.54
	<1 μm	1.19	14.53	27.22	42.94
Cu	Total	1.52	134.19	4.95	140.67
	<10 μm	1.45	84.97	3.83	90.25
	<2.5 μm	1.31	19.5	2.76	23.57
	<1 μm	1.29	8.28	2.54	12.11
Fe	Total	12.08	50,341.32	145.31	50,498.71
	<10 μm	6.6	29,772.04	116.14	29,894.78
	<2.5 μm	2.49	5,700.79	97.76	5,801.04
	<1 μm	2.38	2,302.31	90.29	2,394.98
Mn	Total	1.44	965.96	5.88	973.28
	<10 μm	1.44	573.15	5.6	580.19
	<2.5 μm	1.36	112.98	4.82	119.16
	<1 μm	1.27	46.49	4.6	52.37
Ni	Total	1.37	71.43	35.27	108.07
	<10 μm	1.36	43.3	27.47	72.13
	<2.5 μm	1.25	10.45	25.15	36.85
	<1 μm	1.24	4.96	23.77	29.98
Pb	Total	0.32	774.54	11.6	786.46
	<10 μm	0.32	490.57	10.7	501.59
	<2.5 μm	0.11	112.29	10.01	122.41
	<1 μm	0.11	47.9	9.81	57.82
Zn	Total	270.43	789.91	35.05	1,095.38
	<10 μm	111.45	516.45	28.41	656.31
	<2.5 μm	88.71	170.2	26.66	285.57
	<1 μm	56.82	102.2	25.65	184.67

[a] Emission rates are in kg/d.

been obtained using cascade impactors. *Milford and Davidson* [1985] and *Davidson and Osborn* [1986] summarize trace metal size distributions recorded before the early 1980s. They note that many trace elements, including Cr, Cu, Ni, Zn and Pb, have aerodynamic mass-median diameters less than 2 μm (weighted over all sizes), and generally exhibit bimodal mass distributions (when plotted as *dM*/*dlogD*). The dominant peak is found in the range of 0.5–1 μm, with a smaller peak at about 3–5 μm.

[27] *Lyons et al.* [1993] also present size distributions for several trace metals measured at two locations in the Los Angeles area. The distributions for Cu, Zn and Pb reveal three modes, in the size ranges from 0.075 to 0.26 μm, 0.5 to 1 μm, and 2 to 4 μm. The mode at 0.075–0.26 μm is a nucleation mode, probably associated with fresh emissions from vehicles operating near the field sites. The mode at 0.5–1 μm appears to represent either primary emissions or grown particles (accumulation mode). The size distributions for Ni, however, are bimodal with a broad peak below 0.5 μm, and a second peak in the 2–4 μm range, as observed by *Milford and Davidson* [1985].

[28] To describe the mass mode at 0.5–1 μm detected by *Lyons et al.* [1993] and noted by *Milford and Davidson* [1985], we distribute the submicron emissions of Cu, Zn and Pb using a lognormal size distribution with a geometric mass-mean diameter of 0.7 μm (as opposed to 0.32 μm, as stated above) and standard deviation of 1.8 (compared to 2.16). As before, the ultrafine particle mass is incorporated within the accumulation mode. To represent submicron Ni emissions, the broader baseline urban lognormal distribution (mean size of 0.32 μm and standard deviation 2.16) is used. Like Zn, Cr arises from a large number of common industrial and fugitive sources. Hence, the Cr submicron emission size distribution is chosen to be the same as that for Zn. Again, all of these lognormal functions are truncated at 1 μm, with the numbers of particles renormalized to preserve the total submicron mass emission.

[29] To confirm that the submicron emissions are "preprocessed" into accumulation mode particles as they disperse to the dimensions of the model grid, we conducted sensitivity tests using various submicron emission size distributions together with the fully interactive SMOG treatment of microphysics and chemistry. In an extreme case, all of the submicron particles were assumed to be injected into the smallest model size bin (0.01–0.02 μm). The trace metals were transferred into the accumulation mode between 0.1 and 1 μm on a timescale of several hours via coagulation and condensation processes. In these simulations, the mean diameter of the accumulation mode was somewhat smaller than those observed by *Whitby and Sverdrup* [1980]. This is not surprising since the initial period of intense coagulation in the vicinity of local sources is not included (the initial emissions are already diluted over the model grid in these calculations). Hence, the longer simulated timescale for the growth of trace metals into the accumulation mode is offset by the initial dilution of the emissions. It is also possible to partition a fraction of the initial particles into an ultrafine mode, with this fraction estimated using the results of our sensitivity runs (corresponding to fresh local emissions that have not had a chance to coagulate). This fraction (in terms of mass), however, is very small based on our simulations (and also as recorded by *Whitby and Sverdrup* [1980]). Moreover, because the deposition of trace metals is dominated by relatively large particles, as discussed in subsequent sections, the deposition rates and size distributions are not sensitive to the small residual mass in the ultrafine mode. It follows that the use of "preprocessed" submicron metal emissions offer a reasonable approach for dealing with the structure of the current inventory.

3.3. Summer and Winter Cases

[30] The local climate in Southern California is primarily controlled by large-scale pressure systems, especially the semipermanent high over the North Pacific Ocean [*DeMarrais et al.*, 1965]. Crucial to the dispersion of air pollution in this region are thermally forced winds, including sea-land breezes and mountain-valley flows, as well as winds channeled by terrain [*Lu and Turco*, 1994, 1995; *Wakimoto and McElroy*, 1986]. The strength and relative positions of the Pacific high to the west of southern California and a thermal low to the east determine the pressure gradient over the area throughout most of the year. During the summer months, Southern California is under the eastern edge of the high pressure, and light synoptic winds, clear skies and intense sunshine are the norm. An elevated temperature inversion is present almost continuously, both day and night, over the warm half of the year.

[31] In the winter months, the center of high pressure moves to a southwest position, allowing Pacific storm fronts to penetrate the area. The most frequent synoptic regime in winter is characterized by an additional surface high-pressure cell centered northeast of Southern California over the Great Basin (the high plateau east of the Sierra Nevada Mountains and west of the Rocky Mountains, encompassing most of Nevada and Utah). The clear winter skies that accompany this regime allow the surface air layer to cool radiatively during long nights, leading to the formation of a shallow ground-based temperature inversion. Transitional, and often less stable, meteorological regimes occur most often between the summer and winter seasons.

[32] In this study, we utilize seasonally averaged meteorological conditions to simulate trace metal dispersion and deposition across the LAB. Composite upper-air soundings were obtained from three meteorological stations around the LAB: DRA (Desert Rock, NV), KNX (Miramar, San Diego, CA), and VBG (Vandenburg Air Force Base, Lompoc, CA). Each of these soundings was averaged over two periods: from 1 July to 31 August, 1998, and from 1 November 1998 to 31 January 1999, to represent mean summer and winter conditions, respectively. These average soundings are used to initialize summer and winter simulations characteristic of the region, which are referred to below as the summer and winter baseline cases. In addition, events such as Santa Ana winds are significantly different from the mean situations, but occur at a much lower frequency and thus exert only a modest influence on total annualized trace metal deposition rates (with a relatively larger impact in coastal areas).

[33] The predominant daytime wind flow observed in the summer is the southwesterly sea breeze that carries pollutants from major sources in western Los Angeles toward the San Fernando Valley, into the eastern basin, and through mountain passes (Figure 2). Onshore flow acts to improve air quality in coastal and near-offshore regions. By contrast, nocturnal summer winds become light and unorganized

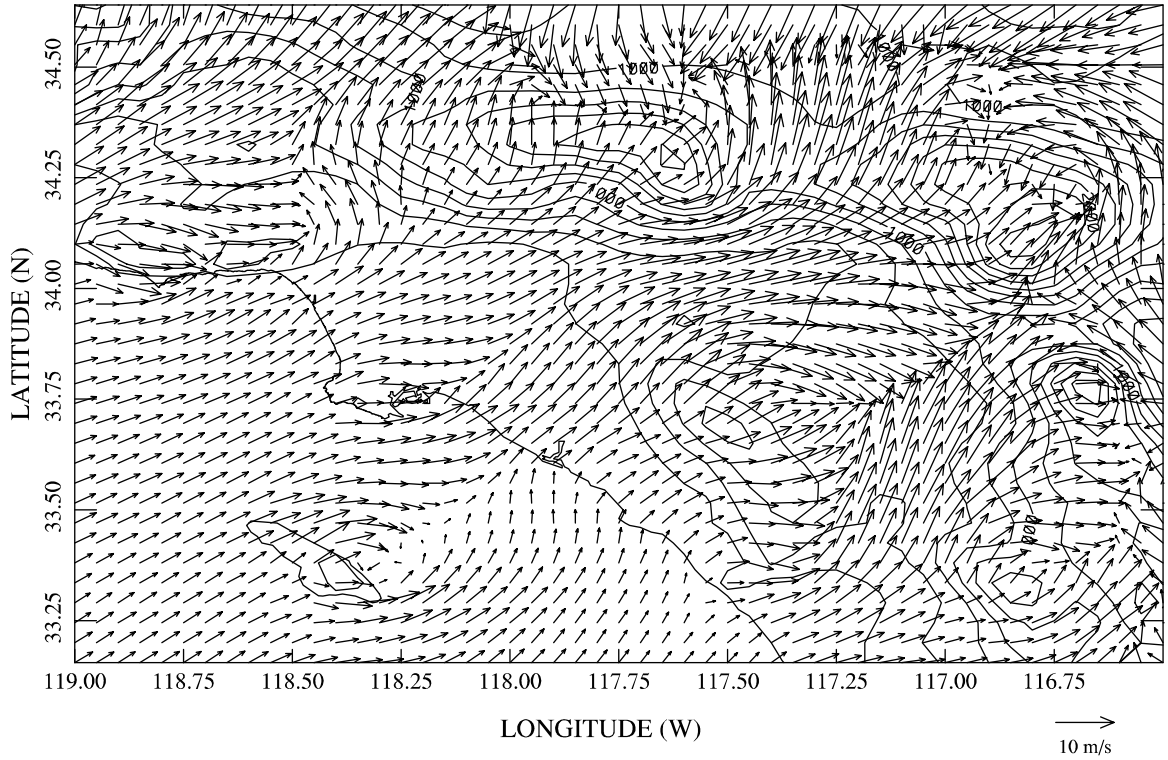

Figure 2. Simulated surface winds during a typical summer afternoon (at 1600 PST). The vector field is dominated by strong land-sea breezes and upslope mountain winds. The length of the wind vector defines the wind speed, as calibrated on the figure.

across the basin and at the coast, in both the simulations and AQMD data. In the winter, the daytime sea breeze has a flow pattern similar to that in the summer, but with a much weaker intensity. The nighttime winter winds have a stronger easterly and northeasterly offshore component due to drainage from the local mountains and land breeze (Figure 3). The land breeze is driven by radiative cooling of land surfaces during the long winter night. The offshore circulation extends over the warmer ocean surface, carrying pollutants in surface air from the coastal plain.

3.4. Comparison of Simulations With Field Measurements

[34] Recently, more intensive PM measurements have been carried out in the South Coast air basin, including the Technical Enhancement Program 2000 (TEP 2000), supporting revisions to the Air Quality Management Plan (AQMP), and the Multiple Air Toxics Exposure Study (MATES II). During TEP 2000, $PM_{2.5}$ and PM_{10} mass loadings, as well as the concentrations of particulate ions, carbon (organic and elemental) and trace metals, were measured at eight sites between August 1998 and July 1999; four of the sites continued to operate after the initial intensive period. MATES II focused on monitoring and characterization of urban toxics [*AQMD*, 2000]. A variety of toxic air contaminants, including trace metals as well as total suspended particle (TSP) mass, was measured over a network of 10 fixed sites once every 6 days for an entire year (April 1998 through March 1999). During this period, three mobile platforms were also used to sample at 14 additional sites for one to two month periods. The TEP 2000 and MATES II sampling sites were located within the LAB based on proximity to populations exposed to poor air quality. As it happens, none of the chosen sites was in the Santa Monica Bay watershed.

[35] To provide additional information on particulates within the Santa Monica Bay watershed, PM measurements were carried out on the UCLA campus from January to December, 1999, as part of a Santa Monica Bay deposition study. These data overlap one three-month period of the MATES II campaign. In analyzing the various data sets, we found that the TEP 2000 data reveal exceptionally high trace metal concentrations in some instances. We were not able to confirm the sources of such high values, which are inconsistent with the other available observations. Hence, we selected the MATES II measurements to calibrate and validate the trace metal simulations for this study. Further, the TSP measurements from MATES are useful for deposition calculations because a significant fraction of the PM mass that contributes to dry deposition is contained on particles larger than 10 μm diameter. This effect has been demonstrated through direct measurements of size-resolved deposition fluxes [e.g., *Tai et al.*, 1999]. PM_{10} and $PM_{2.5}$ data collected at UCLA are also employed in the validations and assessments of deposition onto Santa Monica Bay and its watersheds. The MATES and UCLA field sites providing information for our analysis are identified in Figure 4.

[36] Large uncertainties in model simulations may be associated with emission inventories. Errors in emission rates lead to biases when model predictions are compared against measurements. To minimize the overall impact of uncertainties in emissions, we use MATES measurements to

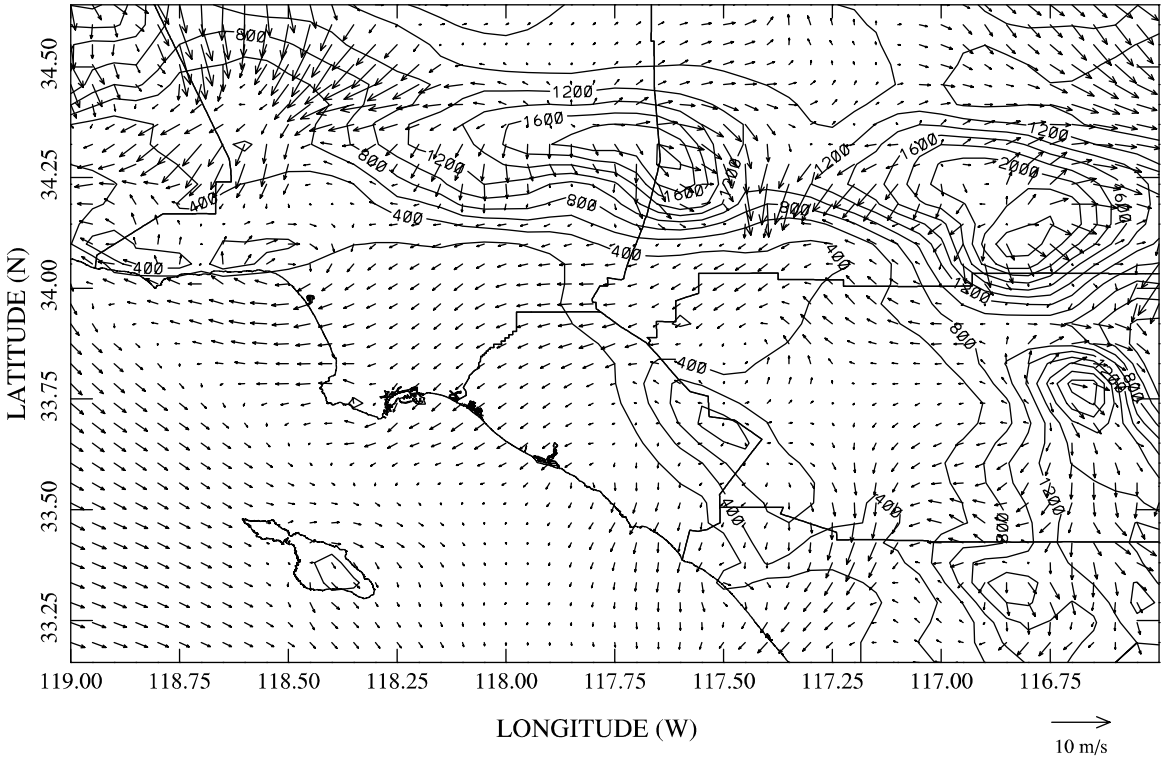

Figure 3. Modeled surface winds during a typical winter night (0400 PST). The fields indicate weak drainage and offshore nocturnal winds throughout the coastal plain. The length of the wind vector defines the wind speed, as calibrated on the figure.

carry out a global calibration of the emissions inventory. Here, we adjust the emissions for each key species to bring calculated air burdens into line with measured mass loadings.

[37] Since trace metals typically do not undergo significant in situ physical and/or chemical transformations, predicted concentrations vary almost linearly with the mean emission intensity. Hence, a uniform calibration factor can be derived for each tracer species by minimizing the bias in its predictions over the network of measurements. First, we calculate the normalized bias, B_n, between the temporally and spatially paired predictions and observations as,

$$B_n = \frac{1}{N}\sum_{i=1}^{N}\frac{p_i - o_i}{o_i}, \tag{7}$$

where N is the number of observational stations, and p_i and o_i are the simulated and observed mass concentrations, respectively, of the tracer of interest at the ith station. The values of p_i and o_i refer to the total airborne mass of a tracer, and thus are not size-discriminated. Further, the tracer mass loadings are usually averaged over a specific interval of time. For example, the raw data (for particulate-borne materials) are typically averaged over a period of 24 or 48 hours (in rare cases, hourly averaged aerosol measurements might be available for certain properties, such as TSP). If a time series of measurements is used, then the calculation in equation (7) can also be summed over the temporal points at each spatial site, i. In the present application, however, we first averaged the time series of measurements at each site in the MATES II network over either the summer or winter period. We then compare this mean observed value to model predictions corresponding, for example, to typical summer or winter meteorological conditions (baseline cases), using an averaging period of 24 hours for the model variables (typically during the second day of a multiday run, to minimize initialization artifacts at earlier times, and forecast drift at later times).

[38] The spatial registration between the observational sites and model grid points is also imprecise. Measurements are collected essentially at a point in space, several meters above the surface. The model, on the other hand, calculates average concentrations (and other parameters) over a 5-kilometer grid within a surface layer that is about 40 meters thick. The nature of point measurements is one reason to time-average the network data prior to making model comparisons. We have interpolated the model variables to the MATES sites using the four nearest-neighbor surface grid point values.

[39] To eliminate the normalized bias from the model calculations, a calibration factor, α, is introduced for each trace metal component predicted by the model. Then α is adjusted until the normalized bias in the calibrated model concentrations disappears, or,

$$\sum_{i=1}^{N}\frac{\alpha p_i - o_i}{o_i} = 0, \tag{8}$$

which is equivalent to,

$$\alpha = \frac{N}{\sum_{i=1}^{N}(p_i/o_i)}. \tag{9}$$

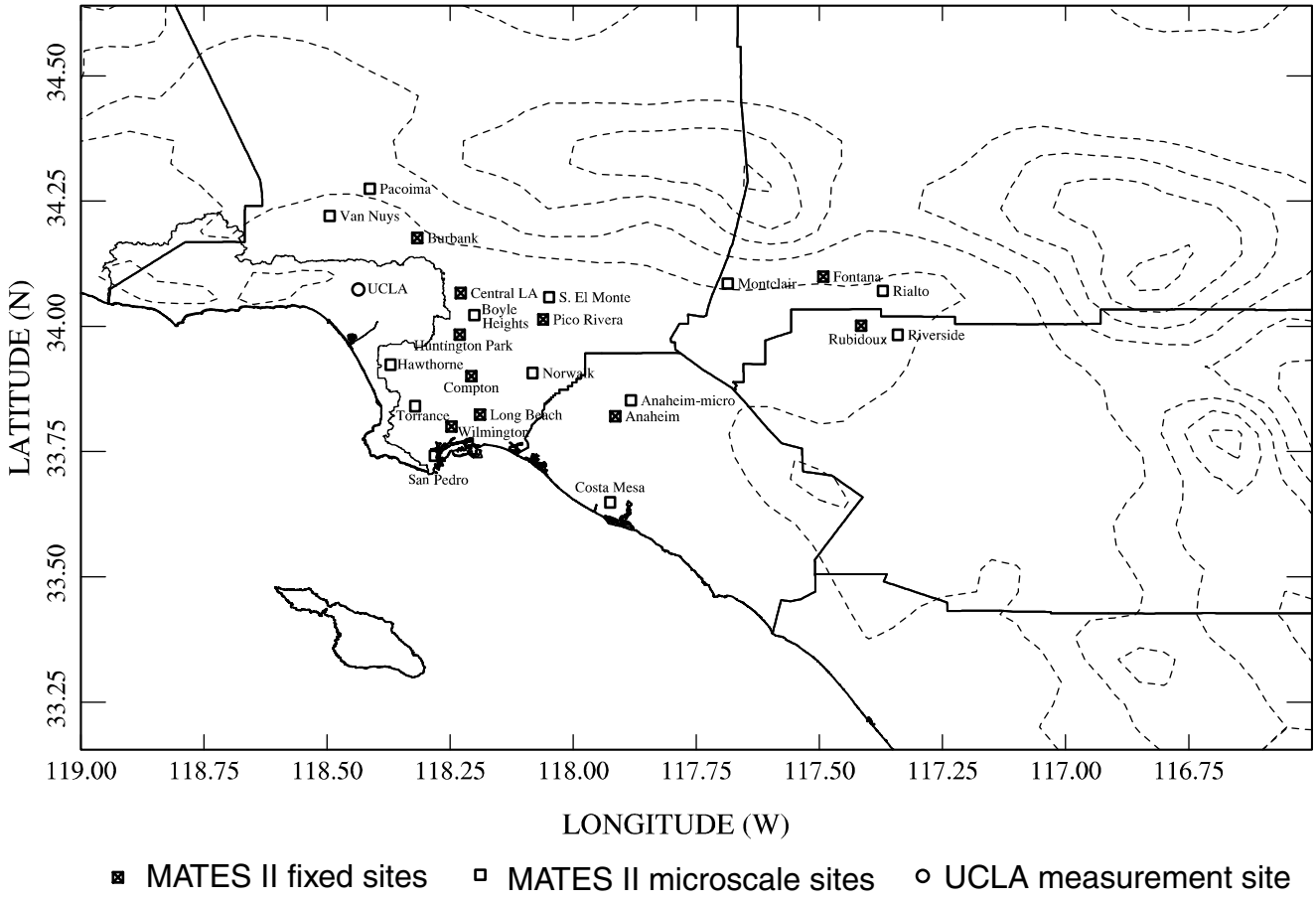

Figure 4. Locations of the primary sampling sites for the 1998/99 MATES II field campaign. An instrument to measure $PM_{2.5}$ and PM_{10} was also operating at UCLA during this period (at the location indicated by an open circle). The sites all fall within the LA Basin, as delimited by the terrain contours. County boundaries for the region are also indicated by solid lines; note that most of the sites are located within Los Angeles County, with relatively few sites in San Bernardino, Riverside, and Orange Counties (clockwise from the upper right-hand corner, respectively).

[40] Assuming perfect linearity in the relationship between trace metal emission rates and predicted mass concentrations, the total emission of each metal can be scaled by its corresponding factor, α. The result is a global inventory that has a nearly zero normalized bias with respect to observational data. In this case, the predictions reproduce, statistically, the MATES measurements. However, the calibration applies to a specific observational network and set of data, as well as particular temporal averaging of the measurements. All sources, moreover, are calibrated by the same factor, and variations in emissions with particle size are ignored. Thus, while it is likely that different trace metal sources have varying degrees of uncertainty, the basic approach taken here does not identify errors in particular emission sources or size ranges.

[41] Table 4 summarizes the derived emission adjustment factors, and the normalized gross errors of the calculated trace metal abundances before and after adjustment of the standard emission inventory (that is, the constituent-specific emission rates estimated for the Southern California region by the SCAQMD). The errors are calculated using mean mass concentrations averaged over all of the MATES II sites. Before adjustment, the normalized gross errors for most of the metals, except Fe, Mn and Ni, arise mainly from the normalized biases (also given in Table 4). Uncertainties in the standard emission inventory as well as systematic errors in the measurements can lead to such biases. Assuming that

Table 4. Trace Metal Prediction Errors and Emissions Adjustment Factors (Summer Conditions)

		Before Adjustment				After Adjustment	
	$\bar{o}$[a]	$\bar{p}$[c]	E_n,[d] %	B_n,[e] %	α[b]	$\bar{p}$	E_n, %
Al	1.302	2.503	113.3	112.5	0.4705	1.178	30.95
Cr	0.008	0.017	135.1	136.1	0.4235	0.007	34.04
Cu	0.037	0.007	77.4	−77.4	4.4150	0.030	38.56
Fe	1.753	1.627	25.7	−0.1	1.0014	1.629	25.74
Pb	0.031	0.037	49.0	39.8	0.7153	0.026	29.20
Mn	0.032	0.032	40.3	17.9	0.8481	0.027	29.09
Ni	0.010	0.010	46.9	8.9	0.9184	0.010	46.21
Zn	0.088	0.056	35.3	−32.5	1.4823	0.083	21.90

[a] $\bar{o}$, observed 24-hour mean concentration averaged over all MATES II sites ($\mu g\ m^{-3}$).
[b] α, adjustment factor derived by eliminating normalized bias.
[c] $\bar{p}$, model predicted 24-hour mean concentration averaged over all MATES II sites ($\mu g\ m^{-3}$).
[d] E_n, normalized gross error (%).
[e] B_n, normalized bias (%).

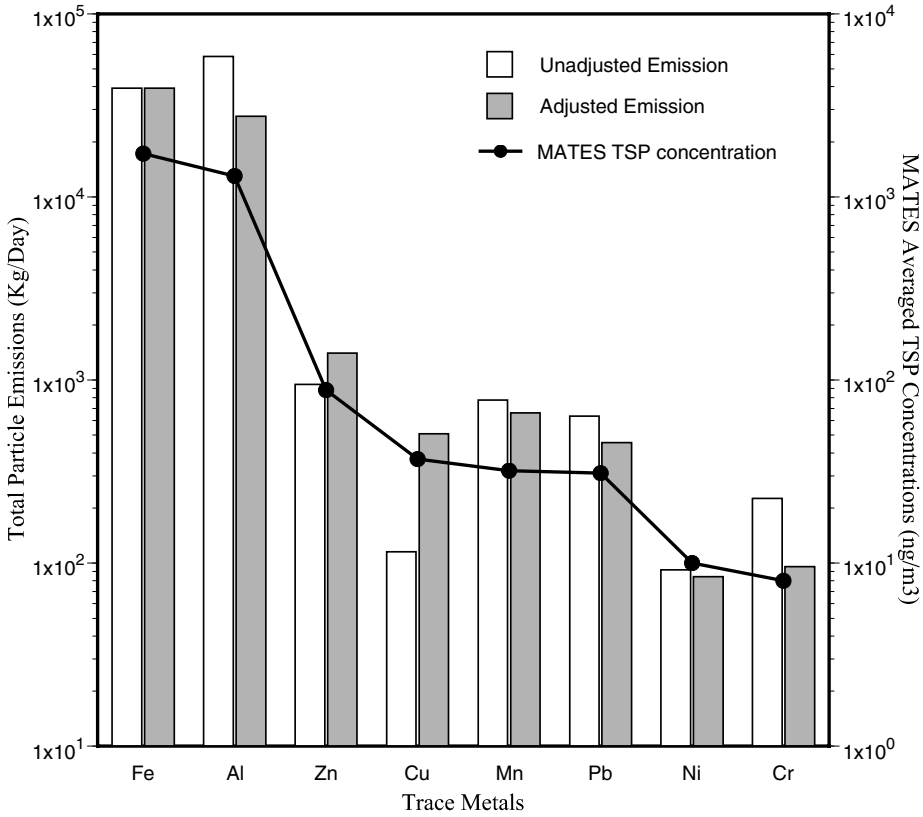

Figure 5. Comparison of standard and adjusted trace metal total emission rates (kg day^{-1}). The standard (unadjusted) emission data were taken from SCAQMD emissions profiles. These values were then adjusted using the approach described in the text. Also shown are the mean particulate-borne trace metal abundances (ng m^{-3}) measured during MATES II (the data are temporally and spatially averaged for each trace metal).

the MATES II measurements are more reliable than the standard emission fluxes, we apply the adjustment factor to the latter for each trace metal. Consequently, the normalized gross errors are considerably improved (Table 4). This approach has been used in the past. For example, *Cass and McRae* [1983] contrasted the relative abundances of trace metals in their fine-particle emissions inventory to the relative elemental abundances derived from ambient monitoring data.

[42] In Figure 5, we compare total basin-wide trace metal emission rates before and after adjustment based on the average airborne concentrations from the MATES II summer campaign. Such adjustments improve the overall agreement between the emission inventory and observed mean airborne concentrations. Accordingly, there is a more consistent agreement between adjusted emissions and mass loadings in Figure 5. We can subsequently use emissions-calibrated model simulations to analyze trace metal deposition rates across the basin (section 4). In this regard, it is more reasonable to calibrate the model against mass concentrations, although uncertainties in the size resolution of the tracer mass are not significantly improved (see the following section).

[43] In Figure 6, contour plot of predicted mean 24-hour-average summertime concentrations of Zn is compared to MATES II site data averaged over a similar period. While the previous calibration procedure normalizes the *mean* concentration over all of the sites, Figure 6 suggests that the *local* values also agree well with field data. For example, the areas of high tracer concentrations in both the eastern and western regions of the LAB, as well as the strong gradient along the coastal margin, are well represented by the SMOG model. The highest abundances of Zn near Wilmington and Fontana are somewhat underestimated by the model, possibly due to local sources that are dispersed over a model grid cell. The extent of agreement at local sites, however, is also demonstrated by the corresponding correlations between site measurements and model predictions in Figure 7. Despite large variability in the recorded trace metal abundances at the MATES sampling stations, the simulated concentrations are well correlated with the mean concentrations measured at these sites across the basin. Typically, the measured and calculated mean concentrations fall well within a factor of two.

[44] The modeled trace metal $PM_{2.5}$ and PM_{10} concentrations at UCLA are compared with measured concentrations in Table 5. The trace metal concentrations on $PM_{2.5}$ and PM_{10} at UCLA represent the annual mean values of the 24-hour-average measurements. By contrast, the modeled concentrations are 24-hour mean values averaged over the summer and winter cases. The calculated and observed metal concentrations agree to within the uncertainty in the measurements, except for zinc on PM_{10}. The sampled

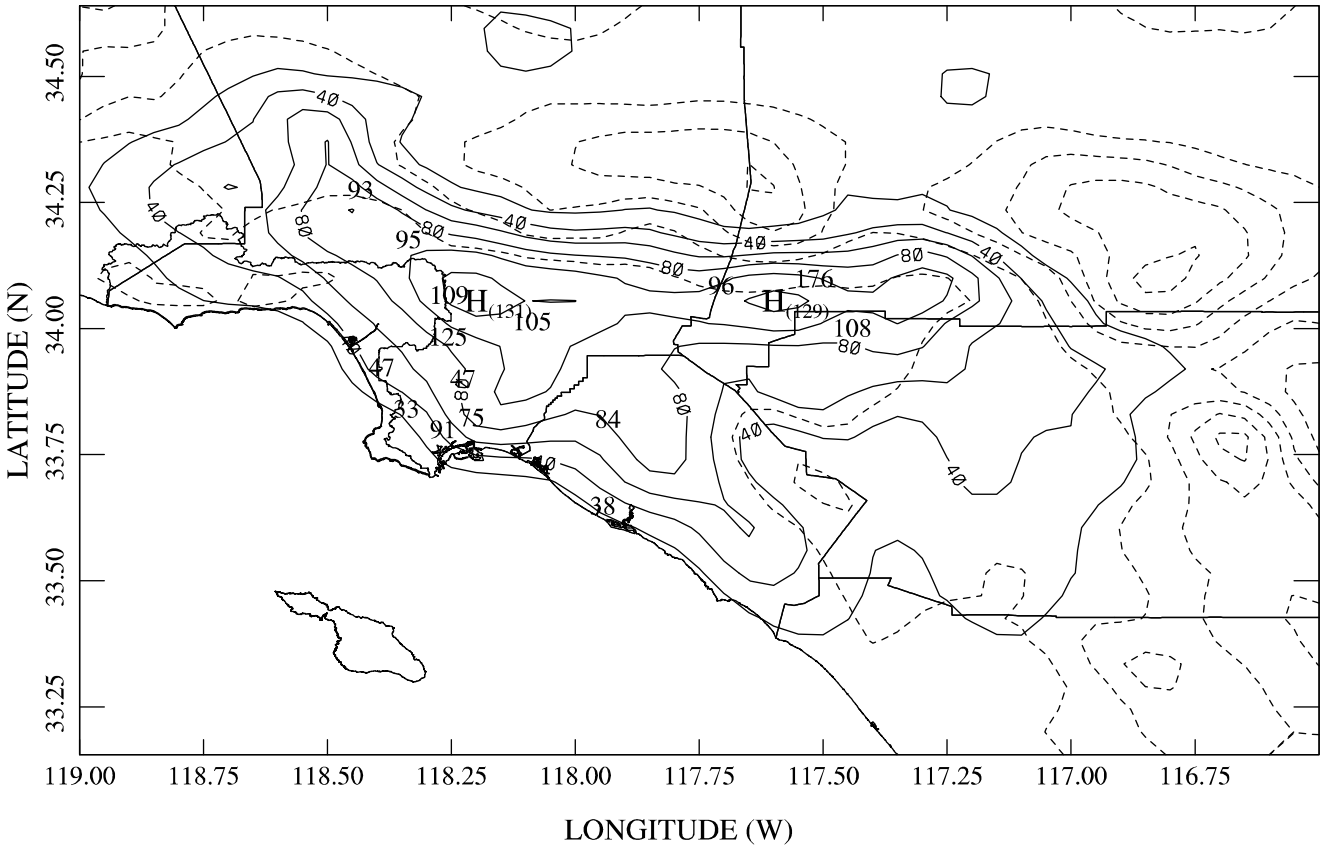

Figure 6. Simulated Zn mass concentrations for the summer season (the summer baseline case described in the text); measurements from the MATES II campaign are shown for comparison. Predicted concentrations are given as isopleths of total mass loading (ng m^{-3}) integrated over the particle size distribution. Isopleths are separated by intervals of 20 ng m^{-3}. The MATES field data are presented as bold numerals representing mean concentrations at each sampling site during the summer baseline period (1 July to 31 August, 1998). All concentrations are expressed as 24-hour average values.

concentrations, in some cases, show very large variability, indicating the strong influence of local sources that were not identified during the sampling period.

4. Trace Metal Deposition in the LA Basin and on the Coastal Ocean Surface

4.1. Trace Metal Concentrations and Deposition Rates in the Los Angeles Basin

[45] Emission, dispersion, and deposition control the distributions of trace metals in the Los Angeles airshed. For many of the species of interest, relatively large emissions and limited ventilation often lead to high concentrations within the LAB. As described in the last section, typical summer Zn mass concentrations in the lowest model layer are illustrated in Figure 6. Similar distributions are found in Pb and other trace metals. These simulations at 5-km resolution reveal the characteristic regional scale spatial variability in the trace metals. The highest concentrations occur within the basin, bounded by the chain of mountain ranges extending from the Pacific Ocean eastward to the desert areas, and with large gradients near the coast as emitted Zn is transported inland. The peak trace metal concentrations appear in areas where the emissions are greatest and dispersion is moderate; for example, adjacent to the San Gabriel Mountains in the northern basin, and the San Bernardino mountains in the eastern basin.

[46] The deposition patterns for trace metals mirror the near-surface mass distributions. For example, the integrated deposition fluxes for Zn corresponding to the average concentrations in Figure 6 are given in Figure 8. The hot spots for deposition are almost exactly superimposed on the hot spots of mass loading. The integrated 24-hour deposition patterns also reveal dispersion gradients extending over distances of tens of kilometers. In a general sense, these results are consistent with measurements obtained by *Lovett et al.* [2000] in New York City, where the concentrations and deposition fluxes of most ionic and metallic species were found to decline significantly with distance from the city center, over a range of about 45 km. Such observations imply that a high degree of regional-scale spatial variability in trace metals and other pollutants requires more than single-point sampling to characterize an urban region properly. That is, measurements within an urban zone are not likely to represent adjacent suburban areas accurately because of large gradients across urban-suburban boundaries; conversely for measurements in the suburbs.

[47] In winter, surface-air trace metal concentrations are usually higher than in summer, in part owing to a narrower

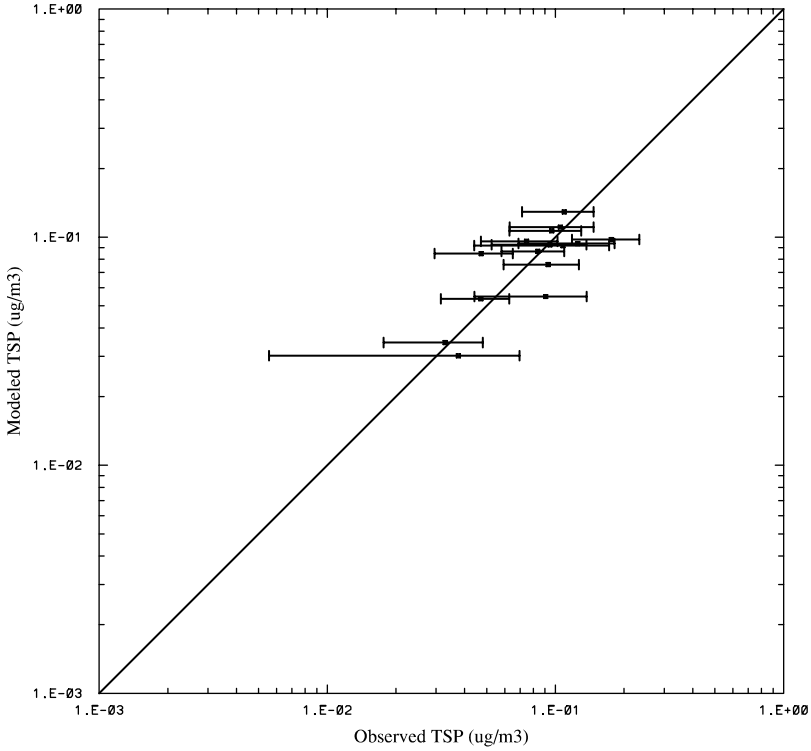

Figure 7. Correlations between simulated and measured Zn mass loadings (for the total suspended particulate, TSP). The observations are from the MATES II field experiment during the summer period (refer to Figure 6 and the text). Filled symbols represent mean 24-hour average concentrations reported at each fixed MATES site (the data plotted in Figure 6), while the error bars indicate one standard deviation in these site data.

boundary layer. However, the spatial patterns of surface concentrations and dry deposition fluxes resemble the summer patterns. This is illustrated for Zn in Figures 9a and 9b (compared with Figures 6 and 8). The highest wintertime mass concentrations and deposition rates are shifted slightly toward the coast, which is a consequence of weaker sea breezes and stronger land breeze in winter. This shift also enhances the amount of zinc deposited along the coastal margin and on coastal waters. The diurnal and seasonal variations in trace metal concentrations and deposition fluxes across the LAB are discussed below using Zn as an exemplar.

4.2. Trace Metal Size Distribution

[48] The dry deposition of an aerosol is strongly size-dependant. For small particles (<0.05 μm diameter), Brownian diffusion governs the rate of transport across the quasi-laminar surface sublayer. However, particles in the size range from 2 to 20 μm diameter are effectively transported across the surface sublayer by inertia. Gravitational settling enhances vertical motion and thus can dominate the dry-deposition of large particles. A characteristic minimum in the deposition velocity occurs in the vicinity of the accumulation mode from about 0.1 to 1 μm diameter, because an effective means for transporting particles across the surface sublayer is lacking in this size range.

[49] As stated earlier, we have assumed that the nucleation mode in the emission inventory is significantly scavenged while dispersing from individual emission sources to distances comparable to the model grid spacing. Accordingly, the modeled particulate typically exhibits two modes in the near-surface trace metal size distribution. An example is shown in Figure 10, where the mass size dispersion and deposition spectrum are given for Zn in surface layer air. The modes in this case are weakly differentiated, with peaks at roughly 0.5 μm and 4 μm diameter. The simulated accumulation mode coincides with typical observations in Los Angeles [e.g., *Lyons et al.*, 1993]. The larger "coarse" particle mode consists of debris raised from paved and unpaved roadways and building sites, including mineral dust and rubber tire particles, as well as windblown dust. Zinc is common in tires and mineral dust. In the submicron size range, timber and brush fires, petroleum heaters, and diesel engine and jet aircraft exhaust are among the major contributors to Zn emissions. Similarly, dusts and fuel

Table 5. Comparisons of Simulated and Measured Trace Metal Concentrations at UCLA

	PM_{10}, ng m^{-3}		$PM_{2.5}$, ng m^{-3}	
	Measured[a]	Modeled	Measured[a]	Modeled
Cr	5.8 ± 5.9	2.4	2.7 ± 4.4	2.0
Cu	16.1 ± 12.6	16.1	5.4 ± 9.6	4.2
Ni	2.1 ± 1.3	2.3	1.4 ± 1.0	1.3
Pb	12.3 ± 31.9	13.8	8.3 ± 26	3.2
Zn	20.2 ± 10.2	43.6	11.3 ± 7.2	17.6

[a] The mean, and root-mean-square variance, of the measurements are indicated.

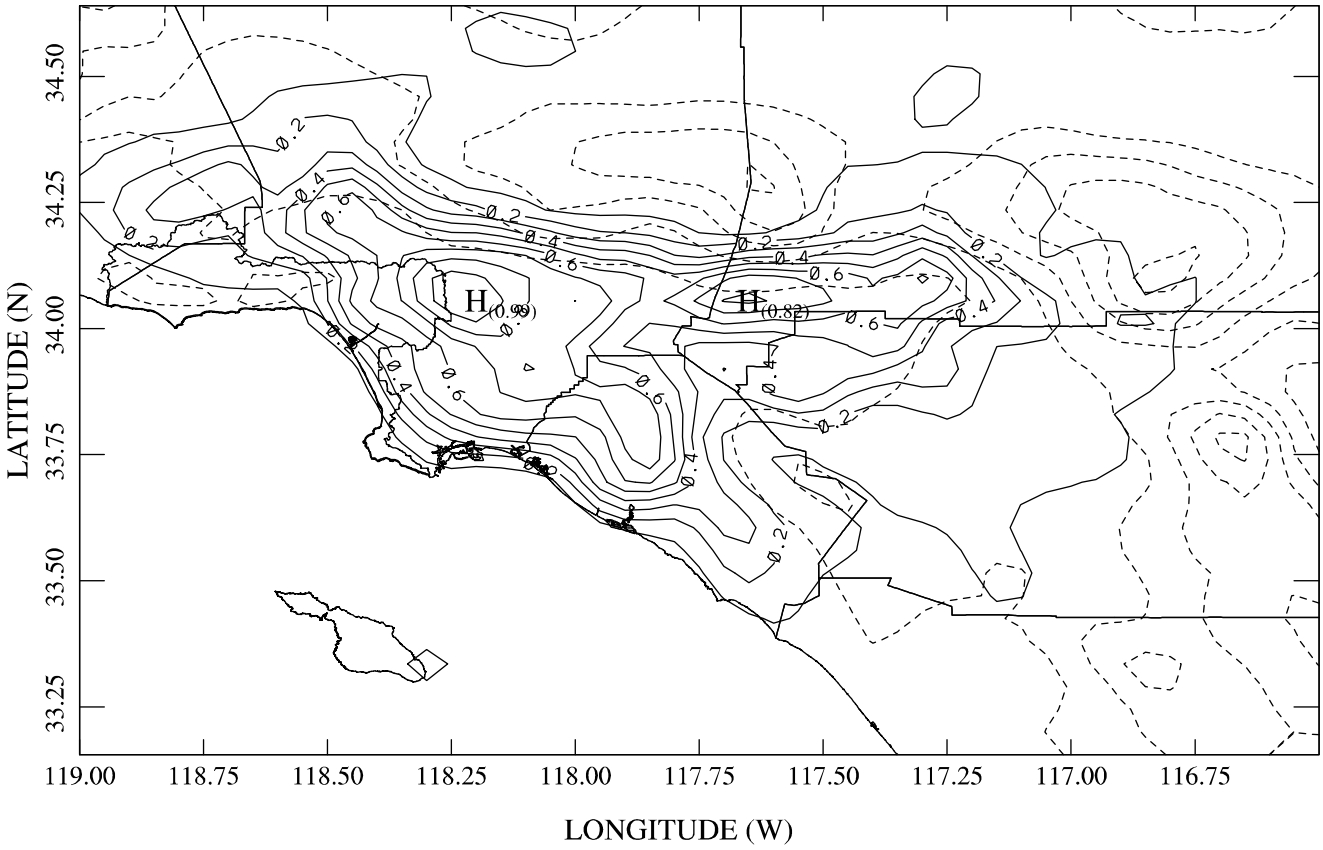

Figure 8. Zinc integrated daily mass deposition (g ha^{-1} day^{-1}) calculated for the summer baseline case (corresponding to the mass loadings in Figure 6). The isopleths give the 24-hour deposition rates separated at intervals of 0.1 g ha^{-1} day^{-1}.

exhausts are the primary contributors of Pb to the coarse and fine size ranges, respectively.

[50] The size spectrum of zinc deposition, integrated over a 24-hour period, is shown in Figure 10b (corresponding to the size distribution in Figure 10a). About 80% of the Zn deposition is associated with particles larger than 10 μm. The deposition flux on particles below 2.5 μm is relatively small owing to the low deposition velocity of particles in the accumulation mode. This result is consistent with size-resolved measurements of trace metal deposition [e.g., *Davidson*, 1977; *Paode et al.*, 1998; *Tai et al.*, 1999].

4.3. Diurnal and Seasonal Variations

[51] The simulations yield significant diurnal variations in trace metal concentrations. This feature reflects daily (predictable) changes in local wind patterns and in the depth of the atmospheric mixed layer, as well as in metal emission rates. Unlike ozone, which is generated in the boundary layer through complex photochemical processes driven by sunlight, trace metal concentrations are more directly connected with their primary emission, vertical mixing, and surface deposition rates. For example, the concentration of a trace metal is nearly proportional to its emission rate, other factors being equal; this is not usually true regarding the relationship between ozone and its precursors.

[52] Figure 11 shows the calculated Zn deposition rates at 4 P.M. on a typical summer afternoon. The surface concentration pattern is similar to the deposition pattern. The corresponding winds at this time are illustrated in Figure 2; the characteristics of the dominant sea breeze and mountain flows are discussed at length by *Lu and Turco* [1995]. It is noteworthy that, between midmorning and late afternoon, onshore and thermally driven winds move fine aerosols (<2.5 μm, including the accumulation mode) from the coastal regions toward the northern and eastern boundaries of the basin. Peak airborne mass loadings and deposition rates for Zn are found along the southern slopes of the San Gabriel and San Bernardino mountain ranges. The trace metals carried on these fine particulates are also transported out of the basin through mountain passes, such as the Cajon and Newhall passes, to the high desert regions beyond. Moreover, the fine particulate is effectively lofted

Figure 9. (opposite) Zinc mass concentration and deposition for the winter baseline case (described in the text). Panel (a): Isopleths of 24-hour average total Zn mass loadings (ng m^{-3}), separated by intervals of 20 ng m^{-3}. The mean of MATES II measurements taken during the period 1 November 1998 to 31 January 1999 are shown as bold numbers at each sampling location, in the same units. Panel (b): The corresponding integrated 24-hour Zn mass deposition (g ha^{-1} day^{-1}), at intervals of 0.1 g ha^{-1} day^{-1}.

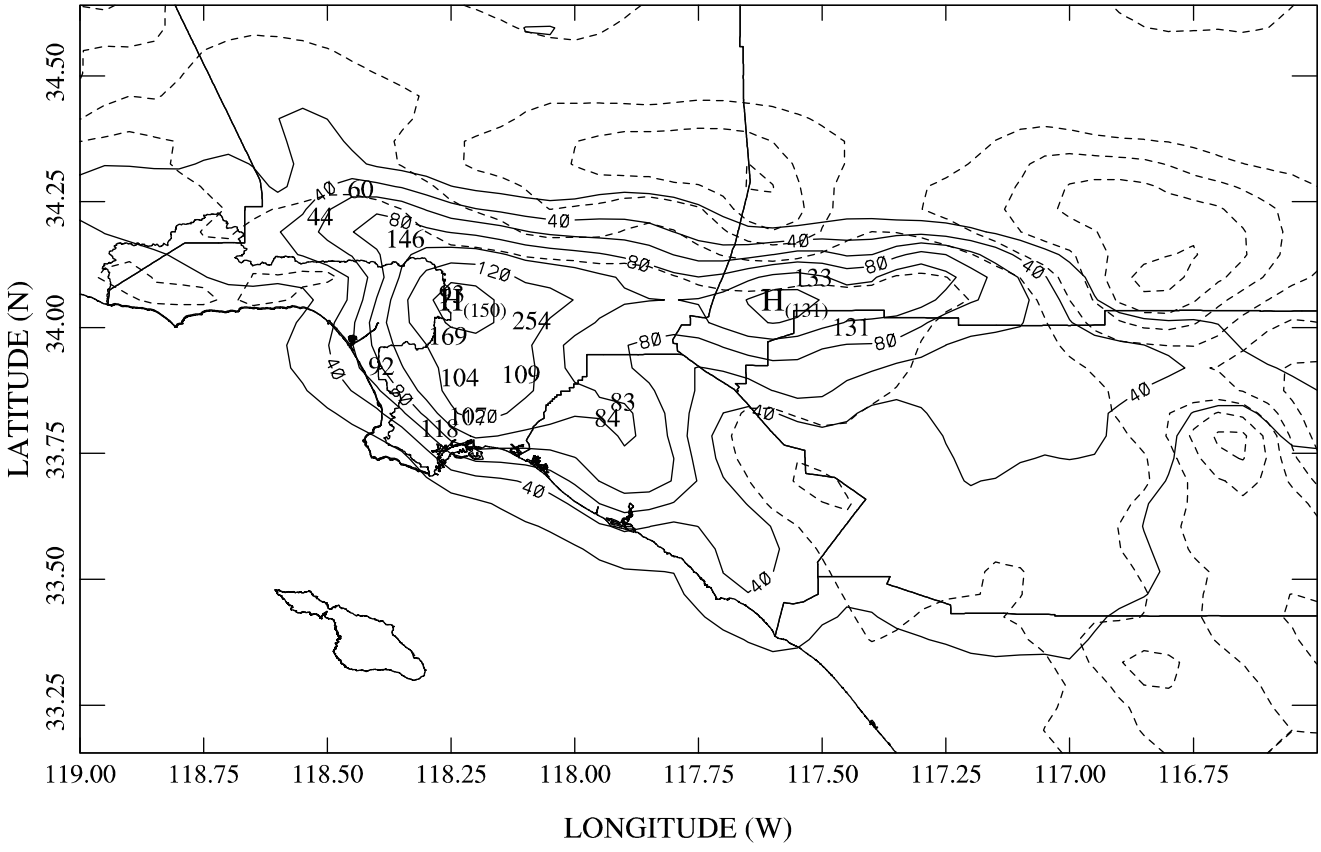
LATITUDE (N)
34.50
34.25
34.00
33.75
33.50
33.25
119.00
118.75
118.50
118.25
118.00
117.75
117.50
117.25
117.00
116.75
LONGITUDE (W)
H(150)
H(131)
40
60
80
120
44
146
254
169
92
104
109
107
118
83
84
133
131

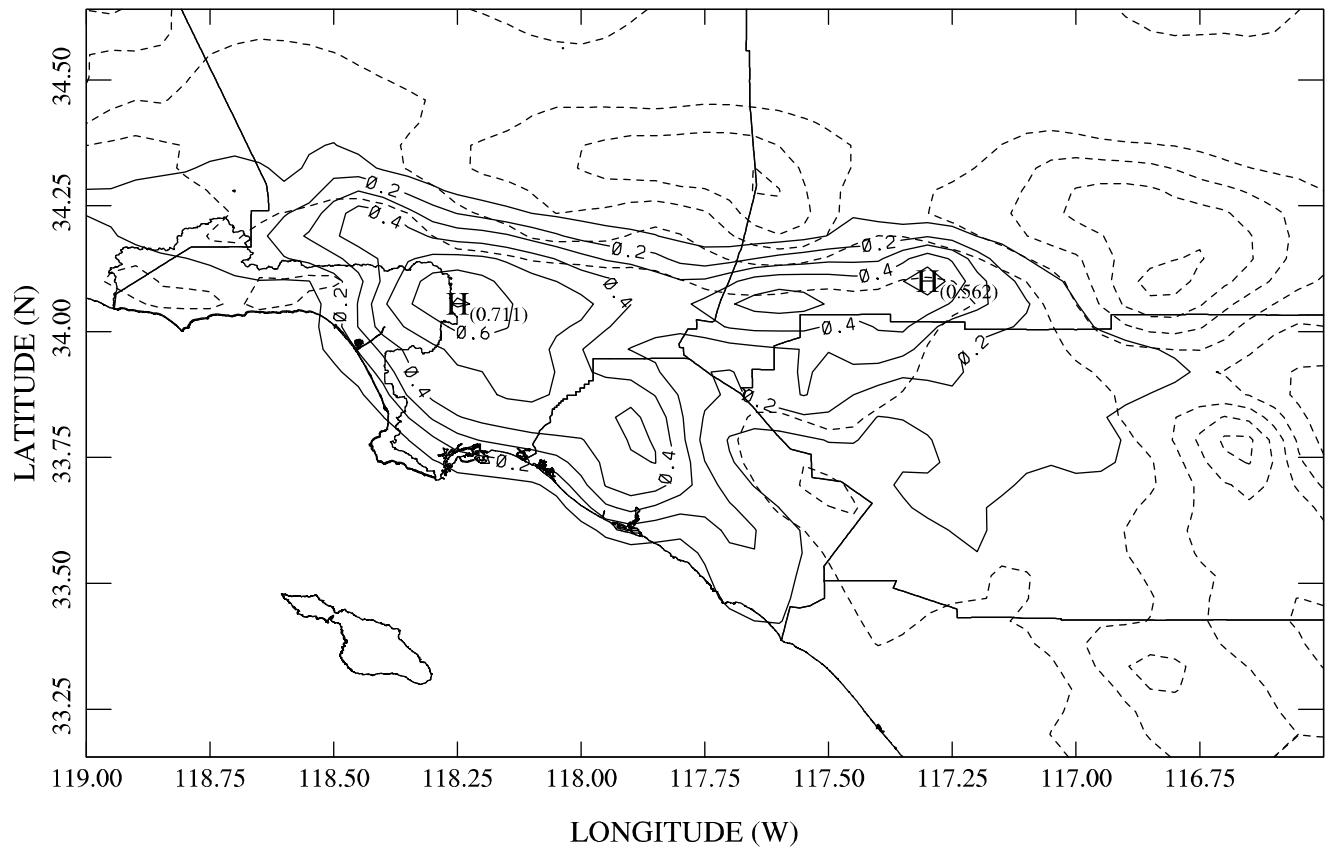
LATITUDE (N)
34.50
34.25
34.00
33.75
33.50
33.25
119.00
118.75
118.50
118.25
118.00
117.75
117.50
117.25
117.00
116.75
LONGITUDE (W)
H(0.711)
H(0.562)
0.2
0.4
0.6

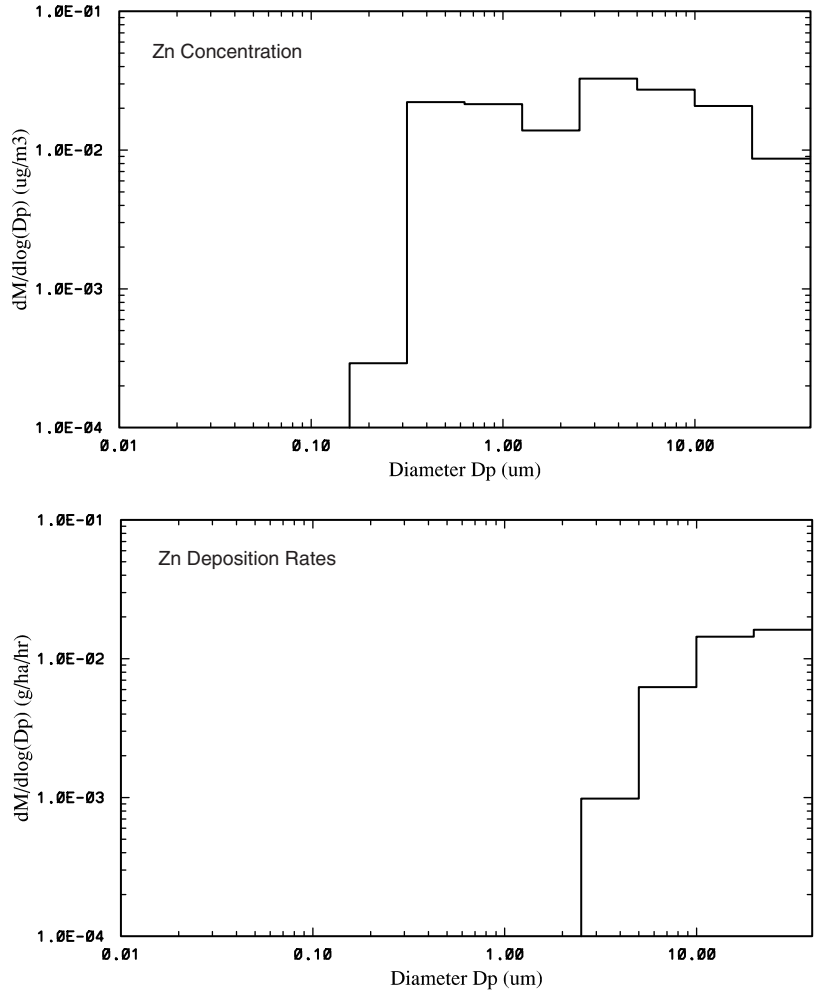

Figure 10. Size-resolved properties of aerosol-borne zinc for the summer baseline case. Panel (a): Mass distribution of Zn versus particle diameter within the surface air layer (averaged over the model domain) ($\mu g\ m^{-3}$); the mass is integrated over each model size bin (Table 1), normalized to the bin width (see below), and plotted as a constant value across the bin. Panel (b): The corresponding size-resolved mass deposition rates ($g\ ha^{-1}\ hour^{-1}$); values represent the mean hourly deposition in a size bin extended over a 24-hour period. Both the mass loading and mass deposition rate are normalized to the logarithmic bin width, defined as $log_{10}(D_2/D_1)$, where D_1 and D_2 are the lower and upper size bin boundaries, respectively.

into the free troposphere by upslope and convergent wind systems [*Lu and Turco*, 1995], and is then subject to long-range dispersion. By comparison, coarse particles (>2.5 μm) have relatively short atmospheric lifetimes ranging from minutes to days, and mainly contribute to the local dry deposition of trace metals within the LAB. Indeed, the afternoon pattern of the Zn deposition flux is the result of dry deposition of coarse particles within several to several tens of kilometers downwind of source regions. The largest deposition rates are confined by the margins of the basin, with peak rates occurring just east of central Los Angeles and near Fontana. In this normal onshore sea-breeze regime, the deposition of trace metals onto coastal waters is not significant.

[53] During the nighttime in the summer, the boundary layer evolves from neutral stability in the early evening to stable conditions as the surface cools. Surface winds are relatively stagnant at night and in the early morning hours, since the sea-land breeze has not yet developed on the coastal plain. Particle-borne trace metal tends to drift slowly, leading to dry deposition near sources. For example, the deposition of zinc at 4 A.M. are illustrated in Figure 12 (which are 12 hours out of phase with Figure 11). Although most of the nocturnal emissions associated with transportation and industrial activity are greatly reduced, damped mixing and dispersion in the stabilized boundary layer actually lead to much higher surface-level trace metal concentrations than during the day. The enhancement is most prominent for the fine particles. On the other hand, mass deposition rates are significantly lower at night and in the early morning hours than during the day. This is caused by two factors: first, the deposition velocities of submicron particles decrease as the stability of the boundary layer increases; second, emissions of the coarse particles that dominate deposition fluxes locally are significantly lower at night.

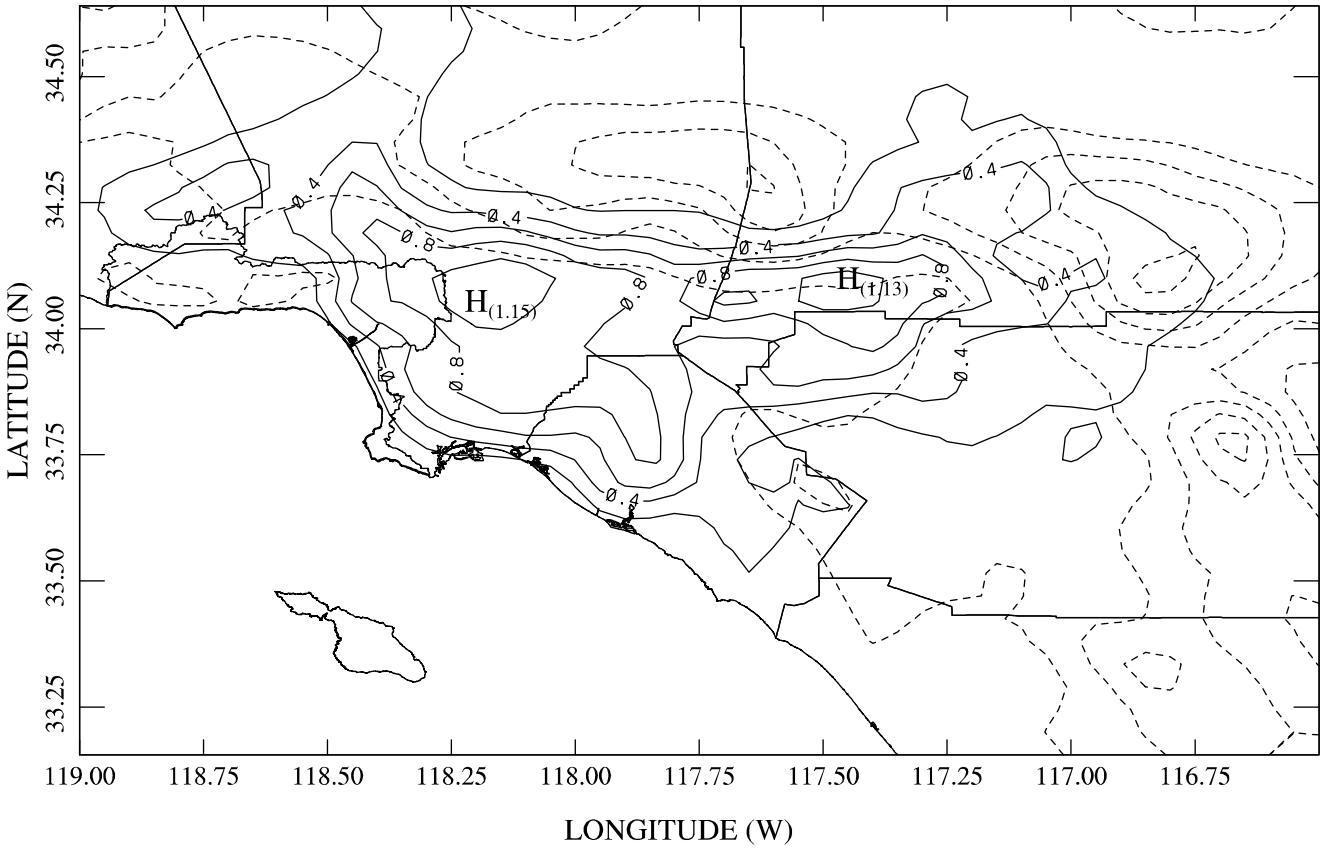

Figure 11. Hourly integrated Zn mass deposition for the period 1500 to 1600 PST for the summer baseline case. Zn mass deposition rates are expressed as an equivalent 24-hour integrated deposition (at the hourly rate), in units of g ha^{-1} day^{-1}, at intervals of 0.2 g ha^{-1} day^{-1}.

[54] An interesting feature of the simulations in Figures 11 and 12 is the maintenance of trace metal deposition along the coast at night, which is related to wind patterns. During the day, the well-developed daytime sea breeze draws particles away from the coastal zone. At night, however, the sea breeze weakens and may even reverse, allowing particulates to be deposited at the land/sea margin. Nevertheless, the deposition fluxes are quite low and confined to the nearshore region.

[55] During the winter season, onshore sea breezes also develop in the afternoon, but are generally weaker than in summer. However, in contrast to the stagnant conditions that evolve within the summer nighttime boundary layer, in winter a nocturnal offshore land breeze frequently builds up near the coast (e.g., refer to Figure 3). The airflow moves particulate matter over coastal waters, leading to greater deposition onto the ocean surface. Figure 13 illustrates this effect for zinc (which can be compared to the equivalent summer calculation in Figure 12). A similar pattern of trace metal deposition has recently been inferred using direct measurements of the enrichment of metals in the surface microlayer of Santa Monica Bay (SMB) compared to the underlying bulk seawater [*Southern California Coastal Water Research Project* (*SCCWRP*), 2000]. Atmospheric dry deposition is a key factor that can lead to the accumulation of airborne pollutants in the microlayer relative to bulk water. Enrichment factors measured for zinc during the fall (transitional) season are shown in Figure 14 [*SCCWRP*, 2000]. The general enrichment pattern is consistent with the deposition maps predicted by the SMOG model. Further, diurnal variations in aerosol-borne trace metal loadings recorded at the coastal margin (Santa Monica Pier) by *Xiong* [2001] are also consistent with the simulations for the SMB area. Xiong observed that the quantity of fine particles, and the abundances of species such as iron and aluminum, increased dramatically during the early morning period (2 to 10 A.M.), during which the winds shifted from a sea breeze to a land breeze orientation.

4.4. Santa Ana Event

[56] Santa Ana winds in Southern California are generally identified as a widespread foehn blowing from the east or northeast. Santa Ana conditions develop when a cold surface high-pressure center builds up over the Great Basin. Strong anticyclonic motion forces a downslope northeasterly flow from the high plateau to the California coastal plain. The resulting compression warms and dries the air reaching Southern California.

[57] Santa Ana winds lead to pronounced changes in the dispersion patterns over the region. As an example of the typical transport and deposition features associated with such an event, the Santa Ana conditions that occurred on 16–17 December 1998 have been recreated. The calculated surface wind fields at 4 P.M. on 16 December and at 4 A.M. on 17 December are shown in Figures 15a and 15b, respectively. During this synoptic event, the northeasterly winds

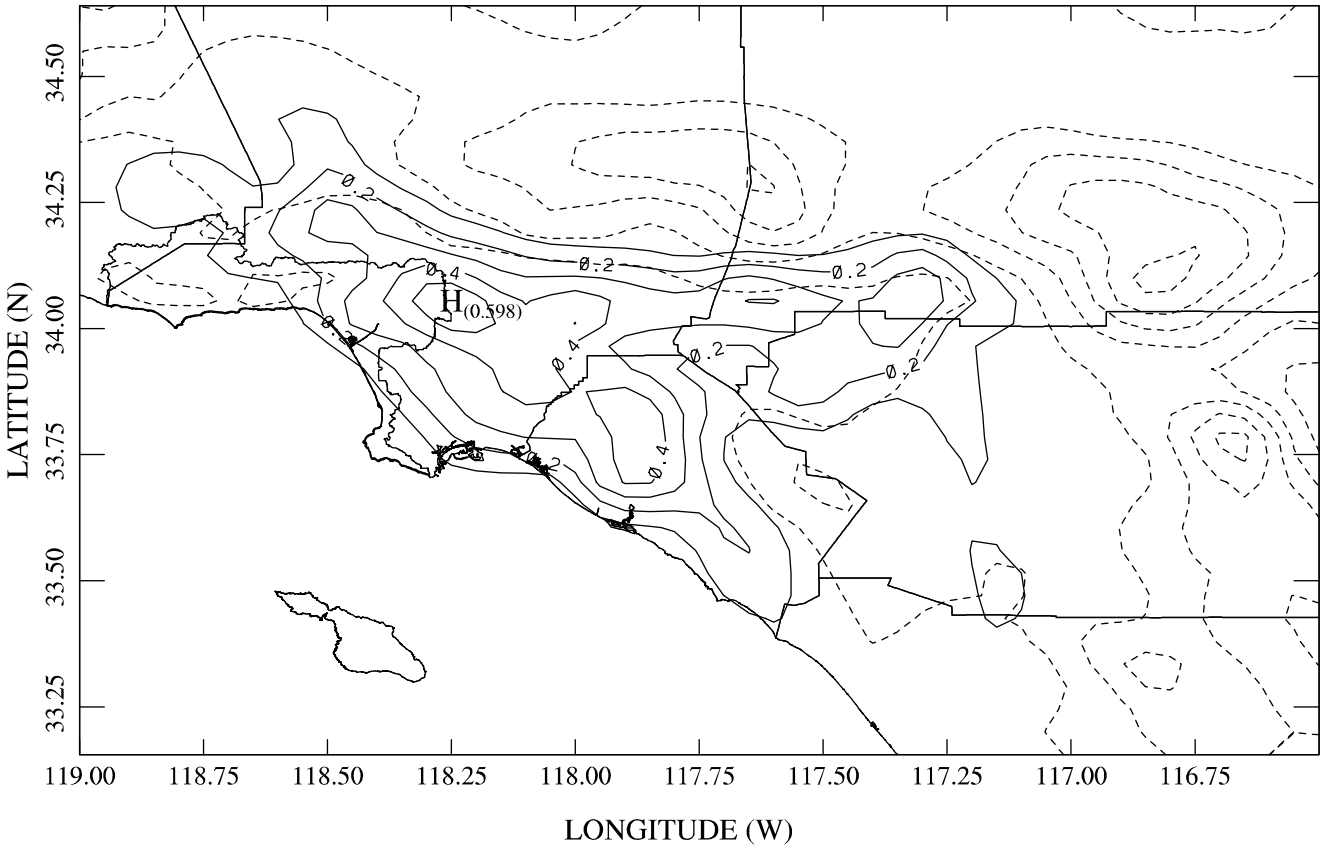

Figure 12. Same as Figure 11, except for the period 0300 to 0400 PST for the summer baseline simulation (i.e., the Zn mass deposition rates are expressed as equivalent 24-hour deposition, in units of g ha^{-1} day^{-1} at intervals of 0.1 g ha^{-1} day^{-1}).

increased during the morning of the first day and reached maximum intensity in the afternoon. Simultaneously, a distinct onshore sea breeze developed near the coast and penetrated well onto the coastal plain. The simulated winds at 4 P.M. (Figure 15a), for example, show the very strong northeasterly flow predominating over most of the inland area, with the sea breeze along the coastal zone of the basin. The sea breeze and Santa Ana winds converge on the coastal plain. A second zone of strong convergence extends northward from Orange County to Riverside County at this time.

[58] At night and in early morning of the second day, the Santa Ana winds are less well organized and the distinct northeasterly flow is not prevalent over the entire region (Figure 15b). Inside the LAB, winds are light and variable. Nonetheless, a general offshore flow characterizes the surface winds along the entire coastline at 4 A.M. This pattern transports pollutants emitted in the Los Angeles area over the adjacent ocean.

[59] Corresponding to the meteorological state in Figure 15, 24-hour integrated mass depositions are shown in Figure 16. Compared to more typical situations (e.g., as in Figure 9b), peak zinc concentrations are distinctly shifted toward the coastal zone, while a massive plume of urban air extends far toward the southwest over the ocean. Hence, the deposition of contaminants on the ocean surface affects a much larger area, and the total atmospheric input of pollutants to coastal waters is greatly enhanced (see below).

[60] Compared to the results in Figure 9, the zinc mass loadings and deposition rates in Figure 16 are substantially reduced in the eastern area of the basin. The peaks along the coastal zone are also moderated somewhat, however, as the emissions are dispersed into the unbounded marine boundary layer. The extended zinc plume over the ocean consists mainly of accumulation mode particles, which is also suggested by the more confined pattern of zinc deposition along the coast.

4.5. Deposition in the LA Basin

[61] Model calculations of atmospheric deposition rates for the chemical species of interest have been used to estimate the mass deposited onto various surfaces in the Los Angeles Basin, including the various counties in the LAB, and the coastal ocean. The resulting annualized total emission and deposition for several trace metals are given in Table 6. To obtain annual integrated deposition, we use the mean summer and winter deposition rates from the previous simulations, and assume that these mean seasonal fluxes are maintained over a 6-month period. The resulting spatially gridded annual deposition is then integrated over each specific subarea. In Table 6, the total deposition for the entire SMOG model domain is also given. Owing to the assumptions made in integrating the deposition over time and space, the values in Table 6 must be considered approximate.

[62] We find that roughly 35–45% (depending on species) of the total trace metal emissions over the model

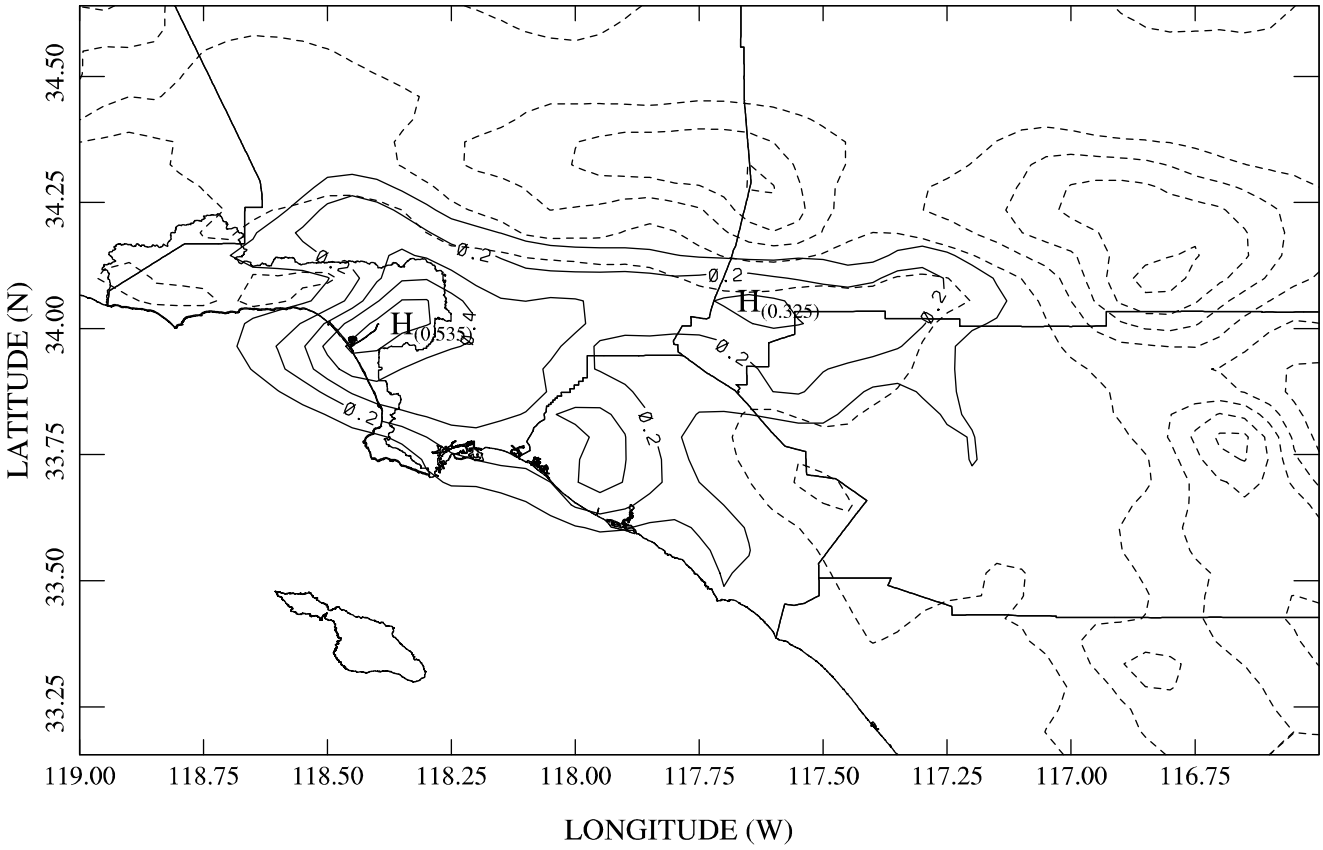

Figure 13. Hourly integrated Zn mass deposition for the period 0300 to 0400 PST for the winter baseline case (contrast with Figure 12). Zn mass deposition rates are expressed as an equivalent 24-hour integrated deposition (at the hourly rate) in units of g ha^{-1} day^{-1}, at intervals of 0.1 g ha^{-1} day^{-1}.

domain are deposited locally within the domain. The remainder is dispersed outside of the simulation domain. Such ''fugitive'' emissions achieve regional to global scales through various long-range transport mechanisms. The local deposition of trace metals across the basin is composed almost exclusively of coarse particles. Aerosols less then 10 μm in diameter contribute about 20% to the total metal deposition in the basin. Fine particles are readily exported from the region because of their relatively long atmospheric lifetimes (days to weeks), especially after being ventilated from the boundary layer into upper air masses.

[63] The model domain used here includes the most heavily polluted regions of the LAB, including the urbanized areas of San Bernardino and Riverside Counties, and all of Orange County. The large fraction of trace metal emissions that occur in Los Angeles County lead to the greatest share of the deposition, roughly 40% of the total regional deposition amount. The deposition in Orange County is also significant, given its smaller populated area. Another 35–40% of the total deposition falls within San Bernardino and Riverside Counties, and is concentrated in the eastern sector of the LAB. In this case, both local emissions and advected pollution contribute to the deposition. The areas of peak deposition are found in Los Angeles and San Bernardino Counties just south of the San Gabriel and San Bernardino mountain ranges.

[64] Since winds from the southwest define the predominant airflow pattern in the basin, the fraction of the local trace metal deposition on the Pacific Ocean (due to dry processes) is only ~2–3% (except for Ni, which is about 8%). However, the marine deposition for typical meteorological conditions is concentrated along the coast, and decreases rapidly with distance offshore. The atmospheric influx of particulate-borne trace metals can still have a significant impact on coastal water quality (refer to Figure 14). These amounts are greatly enhanced during Santa Ana events, when much larger areas of the coastal Pacific Ocean are blanketed by pollution (see the previous section, and Figure 16).

4.6. Trace Metal Deposition on Santa Monica Bay and Its Watersheds

[65] Santa Monica Bay (SMB) is one of the most important natural resources in the Los Angeles Basin, providing more than two million people residing in its watershed with recreation, commercial opportunities, and aesthetic beauty. The bay is home to over 5000 species of birds, fish, mammals, plants, and other wildlife. Santa Monica Bay also bounds the Los Angeles airshed, which generates some of the worst air pollution in the nation. Accordingly, the SMB ecosystem is exposed to trace metals and other toxic contaminants that can cause damage at high concentrations. Despite this threat, virtually no monitoring of air pollution over the bay, or atmospheric deposition onto its surface, has occurred. Moreover, few comparative studies of the different sources of pollutants entering the bay (directly, or

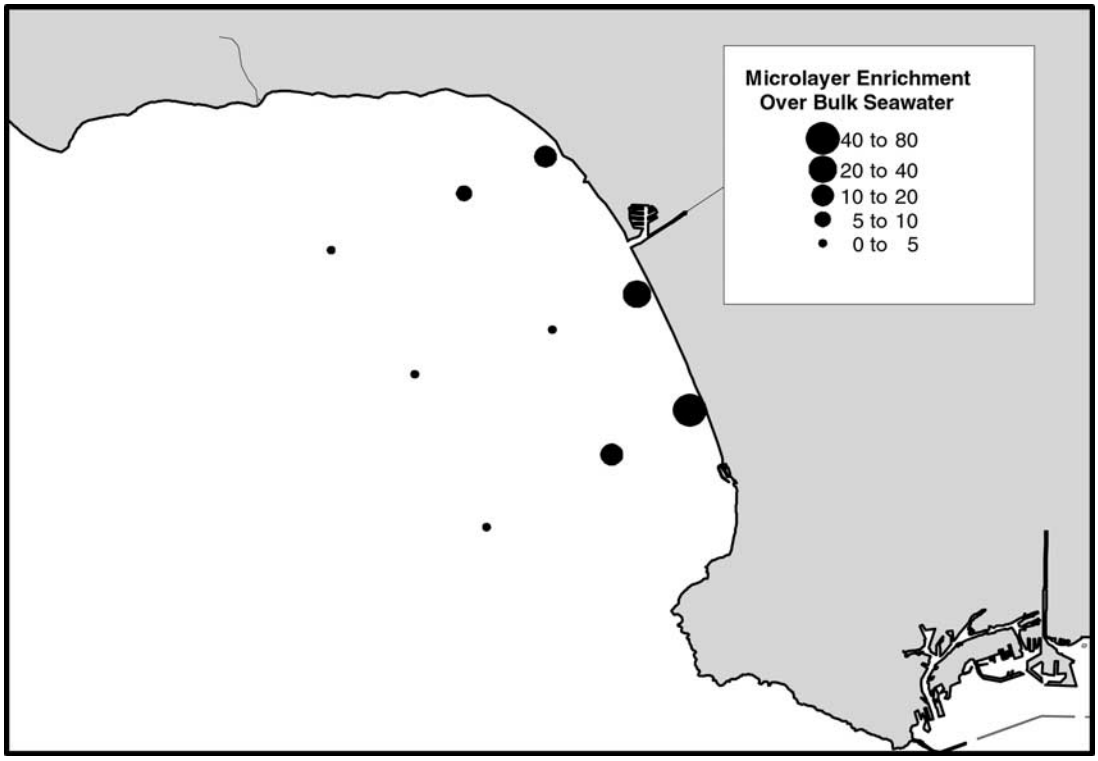

Figure 14. Measured enrichment of Zn in the surface microlayer (compared to bulk water) in Santa Monica Bay. The enrichment factor is defined as the ratio of the zinc concentration in the microlayer to the zinc concentration in the adjacent underlying water column. The observed pattern of microlayer enrichment across the bay is consistent with the simulated pattern of Zn deposition fluxes over the coastal zone.

indirectly via its watersheds) have been carried out. It follows that contaminants introduced through the air, such as particulate metals and certain organic compounds, could prove to be a major source of these materials for SMB.

[66] In the present study, SMOG model simulations are utilized to estimate the various influxes of trace metals to Santa Monica Bay. Local dry deposition rates have already been discussed (e.g., refer to Figures 8, 9, 11–13, and 16), and can be spatially integrated to yield the amounts entering SMB and its watersheds. The annualized source strengths for several of these metals are summarized in Table 7. Here, the contributions from three specific source regions are identified; the source regions are the entire LAB, Los Angeles County, and the SMB watershed itself. Note that these sources are geographically nested, and the total deposition must increase from the smallest to the largest area. Inasmuch as Santa Monica Bay is typically upwind of the Los Angeles Basin, it is not surprising that the annual trace metal deposition onto the bay is much smaller than onto the heavily polluted Los Angeles municipal area. Even so, the quantities of metals deposited from the air are significant within the bay and its watersheds (also refer to Figure 14).

[67] Considering the total direct dry deposition onto SMB, about 70–80% derives from emissions from the watershed areas themselves, and about 95% from sources in Los Angeles County (which effectively incorporates all of the SMB watersheds). The majority of the trace metal deposition in SMB is associated with emission sources adjacent to the bay. Considering the SMB watersheds alone, internal sources are responsible for roughly 70% of the dry deposition. LA countywide emissions account for about 85% of the total deposition onto the watersheds. The differences between the atmospheric deposition due to local sources (summarized above and in Table 7) and the total deposition can be attributed to longer-range transport from more remote areas of the LAB. This source adds about 5% to the direct deposition on Santa Monica Bay, and 15% to the deposition on SMB watersheds. Possible advection of pollutants from outside of the SMOG simulation domain leading to further deposition in the region of Santa Monica Bay has been neglected, but would be expected to increase the total numbers by no more than a few percent.

5. Conclusions

[68] In this study, the SMOG air pollution modeling system has been applied to simulate trace metal concentrations and deposition rates over the entire Los Angeles Basin (LAB), including adjacent coastal ocean surfaces. The metal species of interest are Al, As, Cd, Cr, Cu, Fe, Mn, Ni, Pb, and Zn. Three dominant synoptic states that characterize this region were analyzed: summertime and wintertime mean stable boundary layer conditions dominated by sea and land breezes; and Santa Ana wind events, in which strong offshore airflow occurs. In general, simulated meteorological variables are in accord with typical observed atmospheric parameters in the basin. Corresponding to these

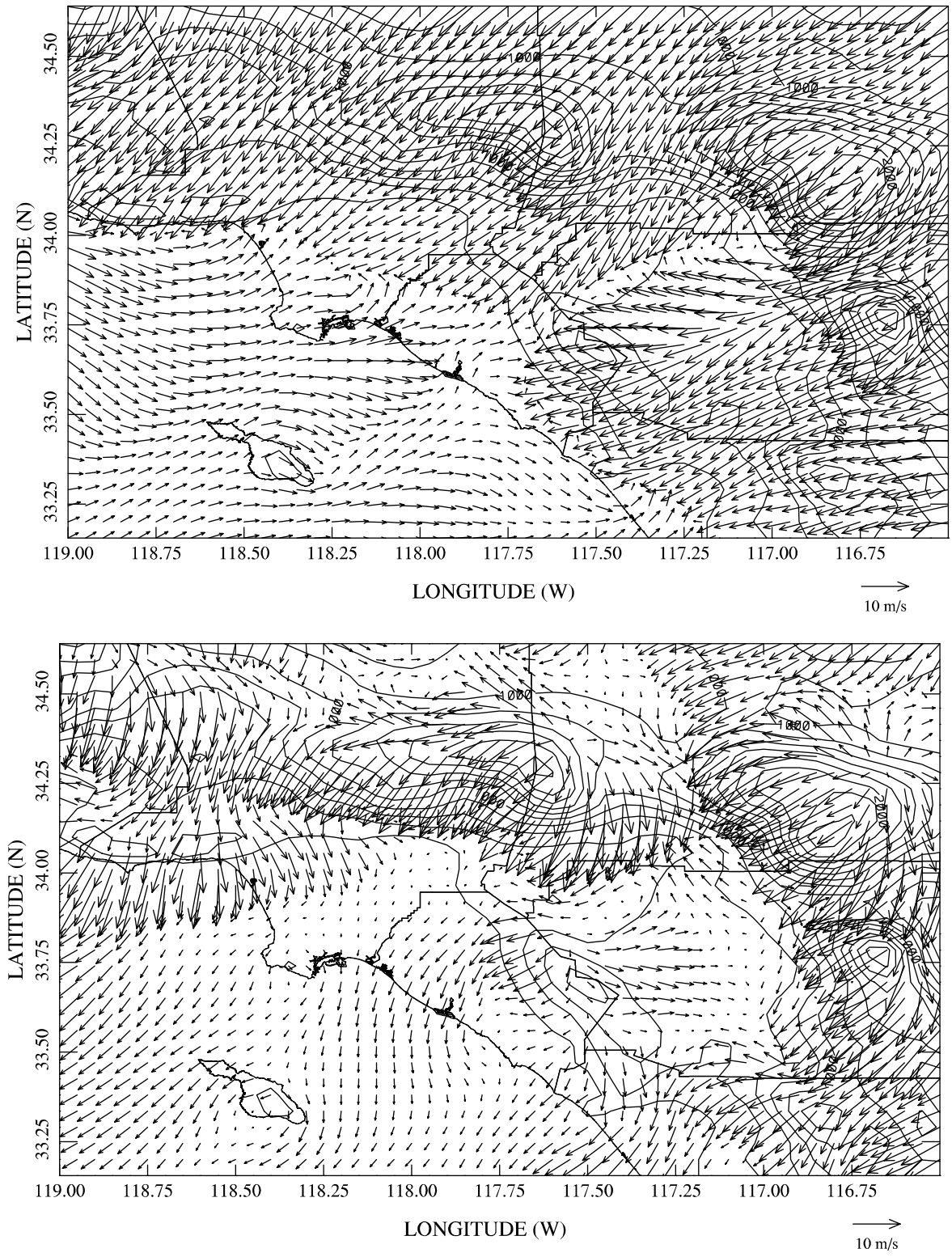

Figure 15. Simulated surface winds during a Santa Ana event in winter, 1998. Panel (a): Afternoon winds at 1600 PST on the first day. Panel (b): Early morning winds at 0400 PST on the second day. The wind strength is measured by the length of the velocity vector, as calibrated against the 10 m s^{-1} bar at the bottom of the graph. Topography and coastline are indicated by solid lines in the background.

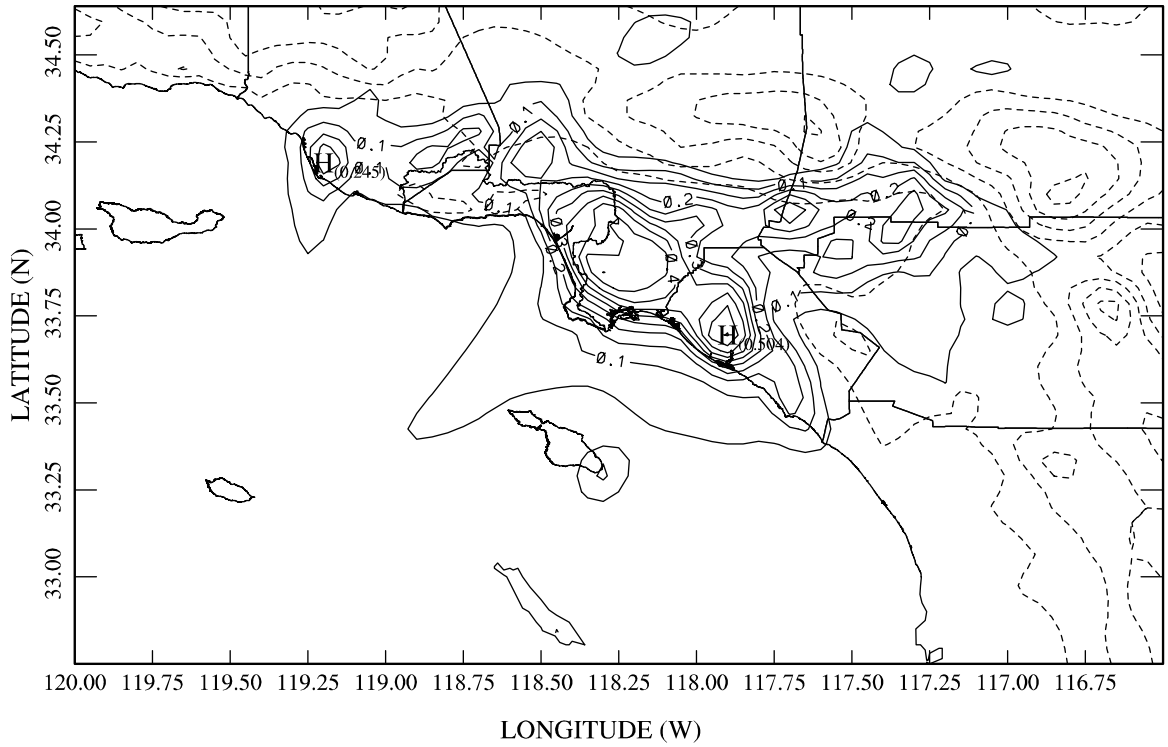

Figure 16. Zn deposition during the winter Santa Ana event depicted in Figure 15 (compare Figure 9b). Isopleths are 24-hour integrated mass deposition in units of g ha^{-1} day^{-1}, at intervals of 0.05 g ha^{-1} day^{-1}.

common meteorological situations, the related trace metal distributions and dry deposition patterns were determined. The present results include the effects of spatially distributed and time-varying sources, as well as the distribution of metals across the entire aerosol size spectrum.

[69] The model simulations have been calibrated using spatially and temporally averaged trace metal mass concentrations derived from total suspended particulate (TSP) measurements taken during the 1998/99 Southern California Multiple Air Toxics Exposure Study (MATES) II field campaign. The calibration processes is designed to minimize potential systematic biases between the mean observed metal concentrations and the standard emission inventory for the region, but is dependent on the accuracy of the MATES II data set. More detailed site comparisons of predicted trace metal concentrations against MATES measurements show overall consistency across the entire LAB, as reflected by differences of less than a factor of 2 between observed and calculated mass loadings at each MATES sampling location for all of the metals treated. Further, the simulated concentrations are in good agreement with independent trace metal abundances for $PM_{2.5}$ and PM_{10} measured at UCLA.

[70] As might be expected, significant spatial variability is found in trace metal mass loadings and deposition fluxes. High concentrations and deposition rates occur near or downwind of major source regions, including freeways and other transportation corridors. Large gradients are also found along the coast, and the mountain slopes of the LAB airshed. The presence of significant spatial variability implies that the extrapolation of measured tracer concentrations and deposition fluxes to regional scales requires more than a handful of sampling sites. Nevertheless, the simulations reveal definite patterns in the (24-hour average) metal distributions, indicating major peaks in the downtown Los Angeles area and in the eastern basin, with secondary

Table 6. Total Emission and Deposition of Trace Metals in the Los Angeles Basin[a]

		Deposition					
	Emission	Total Model Domain	Ocean Surface	Los Angeles County	Orange County	Riverside County	San Bernardino County
Cr	26.62	9.96	0.19	3.94	1.18	1.78	2.14
Cu	140.69	60.29	1.28	24.03	7.81	9.27	13.17
Pb	117.34	51.76	0.98	21.96	6.85	7.19	10.85
Ni	23.68	8.61	0.68	3.40	1.06	1.14	1.62
Zn	424.94	189.17	4.65	79.51	26.21	27.99	39.08

[a] Values are in tons/yr. The deposition is integrated over the regional domains indicated.

Table 7. Deposition of Trace Metals on Santa Monica Bay and Its Adjacent Watersheds From Different Sources[a]

	Deposition to Santa Monica Bay			Deposition to SMB Watersheds		
	Basin Source	LA Source	SMBW Source	Basin Source	LA Source	SMBW Source
Cr	0.067	0.064	0.051	0.527	0.442	0.370
Cu	0.399	0.377	0.275	3.300	2.732	2.227
Pb	0.314	0.298	0.222	2.901	2.419	1.999
Ni	0.078	0.076	0.064	0.382	0.320	0.268
Zn	1.215	1.160	0.872	10.945	9.492	7.890

[a] SMB, Santa Monica Bay; SMBW, Santa Monica Bay adjacent watersheds. Sources are: all sources across the LA Basin, sources within Los Angeles County, and local sources in the SMB watershed. Values are in tons/yr.

lobes extending into the San Fernando Valley and central Orange County regions.

[71] The local deposition of trace metals is dominated by large particles in the simulations. It is found in the case of Zn, for example, that almost all of the deposition is associated with aerosols larger than 2.5 μm diameter. Particles larger than 10 μm account for roughly 80% of the overall deposition of trace metals, including Zn, in the LAB. The deposition of metallic species on coarse particles mainly impacts urban source regions and adjacent areas. Trace components on fine particles, on the other hand, are deposited over regional scales through long-range transport. The present results suggest that routine air quality measurements of PM_{10} and $PM_{2.5}$ are probably inadequate to characterize local to urban scale trace metal deposition rates.

[72] Significant diurnal and seasonal variations in the deposition of trace metals are found for the Los Angeles Basin. These variations are controlled by boundary layer stability, as well as synoptic and regionally induced winds, but also source emission patterns and rates. In summer, the daytime sea breeze transports particles inland, and significant deposition can occur as far away as the deserts beyond the LAB. In the cold season, nighttime land breezes move particulates offshore leading to deposition on the coastal ocean surface. The predicted trace metal deposition patterns closely mimic the observed enrichment of these species in the ocean surface microlayer. During Santa Ana events, strong easterly and northeasterly winds push the urban aerosol plume farther offshore and greatly enhance pollutant fluxes to the ocean surface.

[73] Using model simulations, the first detailed mass budget for trace metals emitted into the Los Angeles urban plume has been constructed. For the species studied here, about 35–45% are deposited locally in and around the LAB. On an annual basis, the deposition of Zn, Pb, Cr, Cu, and Ni amounts to roughly 189, 52, 10, 60, and 9 tons, respectively. Of this total regional deposition, Santa Monica Bay (SMB) and its watersheds receive about 6% annually, which represents a potentially significant source of trace metals for the bay. The landfall deposition amounts to roughly 85% of the total input to the bay and its watersheds. This fraction must be mobilized by precipitation and runoff before contributing to coastal pollution, which occurs regularly during seasonal storms.

[74] Fully 55–65% of the trace metal particulate emissions from the Los Angeles area are found to disperse outside of the region. Of this, a fraction is contained within the boundary layer, and moves as a series of plumes first through mountain passes and then slowly across the arid southwestern United States. Most of the residual emissions, however, are initially injected into the free troposphere (including the temperature inversion above the boundary layer). Here, the material can be carried by jets and fronts over continental to global scales. Aerosol pollutants are also lofted from the boundary layer into the free troposphere by convective processes, and are re-entrained by mixing and subsidence. Eventually, all of the dispersed metals reach the surface via dry or wet deposition.

[75] The present study demonstrates the potential for using detailed urban and regional scale models to determine the anthropogenic contribution of cities to global pollution and climate change. Such an analysis can also provide a means of identifying the mechanisms of transformation and dispersion of emissions from urban zones, and for designing control and mitigation strategies at the source.

[76] **Acknowledgments.** The authors thank Xin Qiu Zhang and Joseph Cassmassi of the Southern California Air Quality Management District for providing particulate emission inventories for 1998, and Paul D. Allen of the California Air Resources Board for clarifying the VOC speciation profiles for this study. The present work was supported by the EPA Watershed Program (EPA R825381) and the California EPA Santa Monica Bay Deposition Study (U.S. EPA/CA Water Resource Control Board 8-108-140-0). One of the authors (R.T.) was also supported by the National Science Foundation (ATM-00-70847) in carrying out this research.

References

AQMD, The Multiple Air Toxics Exposure Study (MATES II) Final Report, South Coast Air Qual. Manage. Dist., Diamond Bar, Calif., 2000.

Arey, J. R., R. Atkinson, B. Zielinska, and P. McElroy, Diurnal concentrations of volatile polycyclic aromatic hydrocarbons and nitroarenes during a photochemical air pollution episode in Glendora, CA, *Environ. Sci. Technol.*, *23*, 321–327, 1989.

Baker, J. E., Atmospheric Deposition of Contaminants to the Great Lakes and Coastal Waters, SETAC, Pensacola, Fla., 1997.

Caffrey, P. F., J. M. Ondov, M. J. Zufall, and C. I. Davidson, Determination of size-dependent dry particle deposition velocities with multiple intrinsic elemental tracers, *Environ. Sci. Technol.*, *32*(11), 1615–1622, 1998.

Cass, G. R., and G. J. McRae, Source receptor reconciliation of routine air monitoring data for trace-metals - An emission inventory assisted approach, *Environ Sci. Technol.*, *17*(3), 129–139, 1983.

Cass, G. R., and G. J. McRae, Emissions and air quality relationships for atmospheric trace metals, in *Toxic Metals in the Atmosphere*, edited by J. O. Nriagu and C. I. Davidson, pp. 145–171, John Wiley, New York, 1986.

Charnock, H., Wind stress on a water surface, *Q. J. Meteorol. Soc.*, *81*, 639–640, 1955.

Davidson, C. I., Deposition of trace metal-containing particles in Los-Angeles area, *Powder Technol.*, *18*(1), 117–126, 1977.

Davidson, C. I., and S. K. Friedlander, Filtration model for aerosol dry deposition — Application to trace-metal deposition from the atmosphere, *J. Geophys. Res.*, *83*(C5), 2343–2352, 1978.

Davidson, C. I., and J. F. Osborn, The sizes of airborne trace metal containing particles, in *Toxic Metals in the Atmosphere*, edited by J. O. Nriagu and C. I. Davidson, pp. 355–390, John Wiley, New York, 1986.

DeMarrais, G. A., G. C. Holzworth, and C. R. Hosler, Meteorological summaries pertinent to atmospheric transport and dispersion over southern California, 86 pp., Weather Bur., U.S. Dep. of Commer., 1965.

Eganhouse, R. P., and M. I. Venkatesan, Chemical Oceanography and Geochemistry, in *Ecology of the Southern California Bight*, edited by M. D. Dailey, D. J. Reish, and J. W. Anderson, Univ. of Calif. Press, Berkeley, Calif., 1993.

Fitzgerald, J. W., Approximation formulas for the equilibrium size of an aerosol particle as a function of its dry size and composition and the ambient relative humidity, *J. Appl. Meteorol.*, *14*(6), 1044–1049, 1975.

Franz, T. P., S. J. Eisenreich, and T. M. Holsen, Dry deposition of particulate polychlorinated biphenyls and polycyclic aromatic hydrocarbons to Lake Michigan, *Environ. Sci. Technol.*, *32*(23), 3681–3688, 1998.

Garratt, J. R., Drag coefficients over oceans and continents, *Mon. Weather Rev.*, *105*(7), 915–929, 1977.
Giorgi, F., A particle dry-deposition parameterization scheme for use in tracer transport models, *J. Geophys. Res.*, *91*(D9), 9794–9806, 1986.
Gray, H. A., G. R. Cass, J. J. Huntzicker, E. K. Heyerdahl, and J. A. Rau, Characteristics of atmospheric organic and elemental carbon particle concentrations in Los Angeles, *Environ. Sci. Technol.*, *20*(6), 580–588, 1986.
Hering, S. V., and S. K. Friedlander, Origins of aerosol sulfur size distributions in the Los-Angeles Basin, *Atmos. Environ.*, *16*(11), 2647–2656, 1982.
Holsen, T. M., K. E. Noll, G. C. Fang, W. J. Lee, J. M. Lin, and G. J. Keeler, Dry deposition and particle-size distributions measured during the Lake-Michigan Urban Air Toxics Study, *Environ Sci. Technol.*, *27*(7), 1327–1333, 1993.
Huntzicker, J. J., S. K. Friedlander, and C. I. Davidson, Material balance for automobile-emitted lead in Los Angeles basin, *Environ. Sci. Technol.*, *9*, 448–457, 1975.
Jacobson, M. Z., Development and application of a new air pollution modeling system. Part III: Aerosol-phase simulations, *Atmos. Environ.*, *31*, 587–608, 1997.
Jacobson, M. Z., and R. P. Turco, SMVGEAR: A sparse-matrix, vectorized Gear code for atmospheric models, *Atmos. Environ.*, *28*, 273–284, 1994.
Jacobson, M. Z., and R. P. Turco, Simulating condensational growth, evaporation and coagulation of aerosols using a combined moving and stationary size grid, *Aerosol Sci. Tech.*, *22*, 73–92, 1995.
Jacobson, M. Z., R. Lu, R. P. Turco, and O. B. Toon, Development and application of a new air pollution modeling system. Part I: Gas-phase simulations, *Atmos. Environ.*, *30*, 1939–1963, 1996a.
Jacobson, M. Z., A. Tabazadeh, and R. P. Turco, Simulating equilibrium within aerosols and nonequilibrium between gases and aerosols, *J. Geophys. Res.*, *101*, 9079–9091, 1996b.
Kaplan, I., and S. T. Lu, Contribution of Atmospheric Contaminants to the Southern California Bight Water Column, Report to the Southern California Coastal Water Research Project, 1993.
Lankey, R. L., C. I. Davidson, and F. C. McMichael, Mass balance for lead in the California south coast air basin, *Environ. Res.*, *78*, 86–93, 1998.
Lo, A. K. F., The direct calculation of fluxes and profiles in the marine surface layer using measurements from a single atmospheric level, *J. Appl. Meteorol.*, *32*, 1893–1900, 1993.
Lo, A. K. F., L. M. Zhang, and H. Sievering, The effect of humidity and state of water surfaces on deposition of aerosol particles onto a water surface, *Atmos. Environ.*, *33*(28), 4727–4737, 1999.
Lovett, G. M., J. J. Bowser, and E. S. Edgerton, Atmospheric deposition to watersheds in complex terrain, *Hydrol. Processes*, *11*(7), 645–654, 1997.
Lovett, G. M., M. M. Traynor, R. V. Pouyat, M. M. Carreiro, W. X. Zhu, and J. W. Baxter, Atmospheric deposition to oak forests along an urban-rural gradient, *Environ. Sci. Technol.*, *34*(20), 4294–4300, 2000.
Lu, R., and R. P. Turco, Air pollutant transport in a coastal environment, 1, 2-dimensional simulations of sea-breeze and mountain effects, *J. Atmos. Sci.*, *51*(15), 2285–2308, 1994.
Lu, R., and R. P. Turco, Air pollutant transport in a coastal environment, 2, 3- dimensional simulations over Los Angeles Basin, *Atmos. Environ.*, *29*(13), 1499–1518, 1995.
Lu, R., R. P. Turco, and M. Z. Jacobson, An integrated air pollution modeling system for urban and regional scales, 1, Structure and performance, *J. Geophys. Res.*, *102*(D5), 6063–6079, 1997a.
Lu, R., R. P. Turco, and M. Z. Jacobson, An integrated air pollution modeling system for urban and regional scales, 2, Simulations for SCAQS 1987, *J. Geophys. Res.*, *102*(D5), 6081–6098, 1997b.
Lyons, J. M., C. Venkataraman, H. H. Main, and S. K. Friedlander, Size distributions of trace-metals in the Los Angeles atmosphere, *Atmos. Environ., Part B*, *27*(2), 237–249, 1993.
McRae, G. J., W. R. Goodin, and J. H. Seinfeld, Development of a second-generation mathematical model for urban air pollution, I, Model formulation, *Atmos. Environ.*, *16*(4), 679–696, 1982.
Milford, J. B., and C. I. Davidson, The sizes of particulate trace elements in the atmosphere - A review, *J. Air Pollut. Control Assoc.*, *35*(12), 1249–1260, 1985.
Paode, R. D., S. C. Sofuoglu, J. Sivadechathep, K. E. Noll, T. M. Holsen, and G. J. Keeler, Dry deposition fluxes and mass size distributions of Pb, Cu, and Zn measured in Southern Lake Michigan during AEOLOS, *Environ. Sci. Technol.*, *32*(11), 1629–1635, 1998.
Paode, R. D., U. M. Shahin, J. Sivadechathep, T. M. Holsen, and W. J. Franek, Source apportionment of dry deposited and airborne coarse particles collected in the Chicago area, *Aerosol Sci. Technol.*, *31*(6), 473–486, 1999.
Pryor, S. C., and R. J. Barthelmie, Particle dry deposition to water surfaces: processes and consequences, *Mar. Pollut. Bull.*, *41*, 220–331, 2000.
Southern California Coastal Water Research Project (SCCWRP), Atmospheric Transport And Deposition of Toxic Contaminants to Santa Monica Bay, CA, Data Report, SCCWRP, Westminster, Calif., 2000.
Shahin, U. M., S. M. Yi, R. D. Paode, and T. M. Holsen, Long-term elemental dry deposition fluxes measured around lake Michigan with an automated dry deposition sampler, *Environ. Sci. Technol.*, *34*(10), 1887–1892, 2000.
Seinfeld, J. H., and S. N. Pandis, *Atmospheric Chemistry and Physics: From Air Pollution to Climate Change*, John Wiley, New York, 1997.
Slinn, S. A., and W. G. N. Slinn, Predictions for particle deposition on natural waters, *Atmos. Environ.*, *14*(9), 1013–1016, 1980.
Tai, H. S., J. J. Lin, and K. E. Noll, Characterization of atmospheric dry deposited particles at urban and non-urban locations, *J. Aerosol Sci.*, *30*(8), 1057–1068, 1999.
Tanner, P. A., P. T. Law, and W. F. Tam, Comparison of aerosol and dry deposition sampled at two sites in Southern China, *J. Aerosol Sci.*, *32*, 461–472, 2001.
Toon, O. B., R. P. Turco, J. Jordan, J. Goodman, and G. Ferry, Physical processes in polar stratospheric ice clouds, *J. Geophys. Res.*, *94*(D9), 11,359–11,380, 1989.
Wakimoto, R. M., and J. L. McElroy, Lidar observation of elevated pollution layers over Los-Angeles, *J. Clim. Appl. Meteorol.*, *25*(11), 1583–1599, 1986.
Wesely, M. L., B. B. Hicks, W. P. Dannevik, S. Frisella, and R. B. Husar, An eddy-correlation measurement of particulate deposition from the atmosphere, *Atmos. Environ.*, *11*(6), 561–563, 1977.
Whitby, K. T., and G. M. Sverdrup, California aerosols: their physical and chemical characteristics, in *The character and Origins of Smog Aerosols: A Digest of Results From the California Aerosol Characterization Experiments (ACHEX)*, edited by G. M. Hidy et al., pp. 477–517, John Wiley, New York, 1980.
Williams, R. M., A model for the dry deposition of particles to natural water surfaces, *Atmos. Environ.*, *16*(8), 1933–1938, 1982.
Wu, J., Wind stress and surface roughness at air-sea interface, *J. Geophys. Res.*, *74*, 444–455, 1969.
Xiong, C., Chemical and morphological studies of marine and urban aerosols, M.Sc. thesis, Univ. of Calif., Los Angeles, 2001.
Yi, S. M., T. M. Holsen, and K. E. Noll, Comparison of dry deposition predicted from models and measured with a water surface sampler, *Environ. Sci. Technol.*, *31*(1), 272–278, 1997a.
Yi, S. M., T. M. Holsen, X. Zhu, and K. E. Noll, Sulfate dry deposition measured with a water surface sampler: A comparison to modeled results, *J. Geophys. Res.*, *102*(D16), 19,695–19,705, 1997b.
Yi, S. M., U. M. Shahin, J. Sivadechathep, S. C. Sofuoglu, and T. M. Holsen, Overall elemental dry deposition velocities measured around Lake Michigan, *Atmos. Environ.*, *35*, 1133–1140, 2001.
Young, D., D. J. McDermott, and T. Heesen, Aerial fallout of DDT in Southern California, *Bull. Environ. Contam. Toxicol.*, *16*, 604–611, 1976.
Zhang, L. M., S. Gong, J. Padro, and L. Barrie, A size-segregated particle dry deposition scheme for an atmospheric aerosol module, *Atmos. Environ.*, *35*, 549–560, 2001.
Zufall, M. J., and C. I. Davidson, Dry deposition of particles to water surfaces, in *Atmospheric Deposition of Contaminants to the Great Lakes and Coastal Waters*, edited by J. E. Baker, SETAC, Pensacola, Fla., 1997.
Zufall, M. J., C. I. Davidson, P. F. Caffrey, and J. M. Ondov, Airborne concentrations and dry deposition fluxes of particulate species to surrogate surfaces deployed in southern Lake Michigan, *Environ. Sci. Technol.*, *32*(11), 1623–1628, 1998.

S. K. Friedlander, R. Lu, K. Stolzenbach, R. P. Turco, and C. Xiong, Institute of the Environment, University of California, Los Angeles, CA, USA. (rongl@atmos.ucla.edu)

K. Schiff and L. Tiefenthaler, Southern California Coastal Water Research Project, Westminster, CA, USA.

G. Wang, Santa Monica Bay Restoration Project, Los Angeles, CA, USA.